The influence of confining pressure and preexisting damage on strain localization in fluid-saturated crystalline rocks in the upper crust

Jessica McBeck[1], Benoît Cordonnier[2], Yehuda Ben-Zion[3], François Renard[1,4]

[1]Njord Centre, Departments of Physics and Geosciences, University of Oslo, Oslo, Norway.

[2]European Synchrotron Radiation Facility, Grenoble, France.

[3]Department of Earth Sciences and Southern California Earthquake Center, University of Southern California, Los Angeles, CA, USA.

[4]Université Grenoble Alpes, Université Savoie Mont Blanc, Université Gustave Eiffel, CNRS, IRD, ISTerre, 38000 Grenoble, France.

Corresponding author: Jessica McBeck (j.a.mcbeck@geo.uio.no)

Key Points:

- Digital volume correlation of X-ray tomograms reveals strain localization in triaxial compression experiments.
- Larger confining pressure promotes localization approaching macroscopic failure.
- More preexisting damage promotes episodes of delocalization.

Abstract

The spatial organization of deformation may provide key information about the timing of catastrophic failure in the brittle regime. In an ideal homogenous system, deformation may continually localize toward macroscopic failure, and so increasing localization unambiguously signals approaching failure. However, recent analyses demonstrate that deformation, including low magnitude seismicity, and fractures and strain in triaxial compression experiments, experience temporary phases of delocalization superposed on an overall trend of localization toward large failure events. To constrain the conditions that promote delocalization, we perform a series of X-ray tomography experiments at varying confining pressures (5-20 MPa) and fluid pressures (zero to 10 MPa) on Westerly granite cores with varying amounts of preexisting damage. We track the spatial distribution of the strain events with the highest magnitudes of the population within a given time step. The results show that larger confining pressure promotes more dilation, and promotes greater localization of the high strain events approaching macroscopic failure. In contrast, greater amounts of preexisting damage promote delocalization. Importantly, the dilative strain experiences more systematic localization than the shear strain, and so may provide more reliable information about the timing of catastrophic failure than the shear strain.

Plain Language Summary

The ability of deformation, such as fractures and strain, to spatially cluster or localize produces a wide range of geologic features on Earth, such as crustal fault networks and plate tectonics. Previous work demonstrates that deformation can evolve toward more localized distributions. However, recent analyses show that deformation can temporarily decrease in localization. These decreases in localization complicate efforts to use the spatial organization of seismicity, for example, as a precursor of approaching large earthquakes. The factors that promote phases of delocalization remain unconstrained. Here, we perform a series of experiments to identify the factors that control the delocalization of local strain events within low porosity, Westerly granite rock cores. We find that both the confining pressure, indicative of depth within the crust, and the amount of preexisting damage of the rock cores control the amount of localization that the strain events experience, and the phases of delocalization. Increasing confining pressure produces more localization of the high strain events. More preexisting damage produces more delocalization.

Key words: localization, strain, triaxial compression, confining pressure, dilation, granite

1 Introduction

The localization of strain along fractures, faults, and shear zones is a fundamental phenomenon of rock deformation (e.g., Rudnicki & Rice, 1975; Lockner et al., 1991; Satoh et al., 1996; Benson et al., 2007; Lyakhovsky et al., 2011; Ben-Zion & Zaliapin, 2019). The ability of deformation to localize from the micrometer- to kilometer-scale allowed the Earth's crust to partition into different volumes, and thus is responsible for plate tectonics (e.g., Gueydan et al., 2014; Mulyukova & Bercovici, 2019). Monitoring the localization of deformation may also be useful for recognizing the acceleration of the preparation phase that leads to catastrophic failure in the upper crust, such as large magnitude earthquakes. In particular, machine learning analyses indicate that tracking the distance between fractures in triaxial compression experiments can help successfully predict the timing of catastrophic failure (McBeck et al., 2020b). Similarly, recent observations show that low magnitude seismicity localized in the final two to three years preceding several M>7 earthquakes in Southern and Baja California (Ben-Zion & Zaliapin, 2020). However, for some earthquakes, the seismicity periodically decreased in localization, or delocalized, in the several months preceding the earthquake. These phases of delocalization obscure the relationship between macroscopic failure and localization, and thereby complicate efforts to forecast the timing of an impending large earthquake using the spatial distribution of seismicity. The factors that control whether a rock or crustal volume may experience phases of delocalization remain largely unconstrained.

To help constrain these factors, we perform a series of X-ray synchrotron tomography triaxial compression experiments and track the localization of the local three-dimensional strains calculated from digital volume correlation. To assess the influence of confining pressure and effective pressure on strain localization, we systematically change the confining pressure from 5 MPa to 20 MPa, and fluid pressure from zero to 10 MPa in the experiments. To assess the influence of preexisting heterogeneities on localization, we introduce a network of preexisting fractures and weaknesses into several of the rock cores by thermal treatment. This set of experiments thus allows comparison of the localization of the strain events in relatively intact and damaged rocks, and in systems with lower and higher confining pressure.

2 Methods

2.1. X-ray tomography triaxial compression experiments

We performed six triaxial compression experiments at beamline ID19 at the European Synchrotron Radiation Facility. We used 10 mm tall and 4 mm diameter cylinders of Westerly granite, which is a low-porosity crystalline rock dominated by quartz, feldspar, and biotite. The mean grain size is 100-200 µm (Aben et al., 2016). The initial porosity is lower than 1%.

We imposed a constant confining pressure in each experiment (5-20 MPa), and constant pore fluid pressure (0-10 MPa) (**Figure 1**) with the Hades triaxial compression apparatus via servo-controlled pumps (Renard et al., 2016). We varied the confining pressure and fluid pressure so that five of the experiments experienced the same effective pressure, confining pressure minus fluid pressure (P_e=5 MPa), and one of the experiments experienced P_e=10 MPa. We applied the same effective pressure to the majority of the experiments because failure criteria such as the Mohr-Coulomb criterion use the effective pressure to predict the stress conditions at failure, and not the confining pressure. **Table** S1 lists all the symbols and notations used here. We increased the axial stress in steps of 0.5-5 MPa until the rock failed with a stress drop, with smaller steps closer to failure. After each increase in axial stress, we acquired an X-ray tomogram within one and half minutes while the core was inside the deformation apparatus. The total time required to acquire a tomogram and increase the axial stress is about three minutes. The varying applied increase in axial stress throughout each experiment produces a mean stressing rate of 0.72 MPa/minute across all of the stress steps of all the experiments, and a range of the mean stressing rate for the individual experiments of 0.27-0.99 MPa/minute.

We deformed intact and heat-treated, or damaged, Westerly granite cores. The crack density produced by thermal heating depends on the temperature, differences in the thermal expansion of the minerals, initial porosity, and the grain size (e.g., Fredrich & Wong, 1986). Heating granite to temperatures above 600°C produces significant increases in the crack density and porosity, and decreases in the P-wave speed and uniaxial compressive strength (Griffiths et al., 2017). We heated the cores with an initial heating rate of 4°C/minute from room temperature to 650°C in an oven, and then for five hours at 650°C, and then with a cooling rate of 4°C/minute to room temperature. The heating and cooling procedures were identical. This heating procedure causes the damaged rock cores to fail at lower differential stresses than the intact rock cores for the same confining pressure and effective pressure conditions. We performed all the experiments at ambient room temperature in the range 22-24°C.

For the experiments that include fluid pressure, we saturated the granite cores in deionized water in a vacuum chamber for two weeks before the experiment. The HADES apparatus includes a pore fluid inlet and outlet at the top and bottom of the chamber that contains the rock sample (Renard et al., 2016). To drive fluid flow and so apply the pore fluid pressure, we set a minor fluid pressure gradient of 0.5 MPa between the pore fluid inlet and outlet.

The low initial porosity and permeability of the intact rock cores may have produced a relatively heterogenous distribution of the local pore pressure at the onset of loading, which could have resulted in a heterogeneous distribution of effective pressure. With increasing differential stress, fractures nucleate and propagate, and the porosity and permeability increase, thereby reducing the potential for such variations in effective pressure. Comparing the differential stresses at failure among the three experiments on intact rocks suggests that the resulting effective pressure was relatively constant for experiments WG19 and WG20 (5 MPa applied effective pressure), despite their varying confining pressures, and higher for experiment WG14 (10 MPa applied effective pressure). In particular, the differential stresses at failure for experiments WG19 and WG20 was 242 MPa and 229 MPa, respectively, and for experiment WG14 it was 287 MPa. Moreover, of the two intact experiments with 5 MPa effective pressure, the experiment with higher confining pressure (WG20) had a lower differential stress at failure than the experiment with lower confining pressure (WG19). If the confining pressure primarily controlled the strength of these rocks, rather than the effective pressure, then the experiment with lower confining pressure (WG19) should have had a lower failure stress than the experiment with higher confining pressure (WG20). These results suggest that the effective pressure exerted the dominant influence on the macroscopic strength, rather than the confining pressure. Consequently, despite the low initial porosity of the intact rock cores, the stressing rate was sufficiently slow to allow the pore fluid to flow to the available pores and fractures, and thereby produce a distribution of local effective pressure that approximated the applied, macroscopic effective pressure.

Following each experiment, we reconstructed the acquired radiographs into three-dimensional volumes. The three-dimensional volumes, or tomograms, are 1600x1600x1600 voxels, and each voxel side length is 6.5 µm. The spatial resolution of the tomograms is within two to three voxel side lengths. During reconstruction, we applied methods to remove acquisition noise. We then reduced the remaining noise in the reconstructed, three-dimensional data using the software Avizo3D™, such as a non-local means filter (Buades et al., 2005). We calculate the macroscopic axial strain done on the rock cores, ε_{zz}, using the height of the rock core identified in each tomogram. Consequently, the spatial resolution and quality of the tomogram influence the calculated ε_{zz}.

In one of the experiments on a damaged core (WG18), a system-spanning, horizontal fracture developed as the core was inserted into the deformation apparatus (**Figure S1**). With increasing axial stress, this fracture closed, and other fractures propagated throughout the core. This large preexisting fracture caused this core to fail at a lower differential stress, and to accumulate more ε_{zz} preceding macroscopic failure than expected, and than the other experiments. This experiment thus represents an endmember of rock deformation within a preexisting highly fractured system.

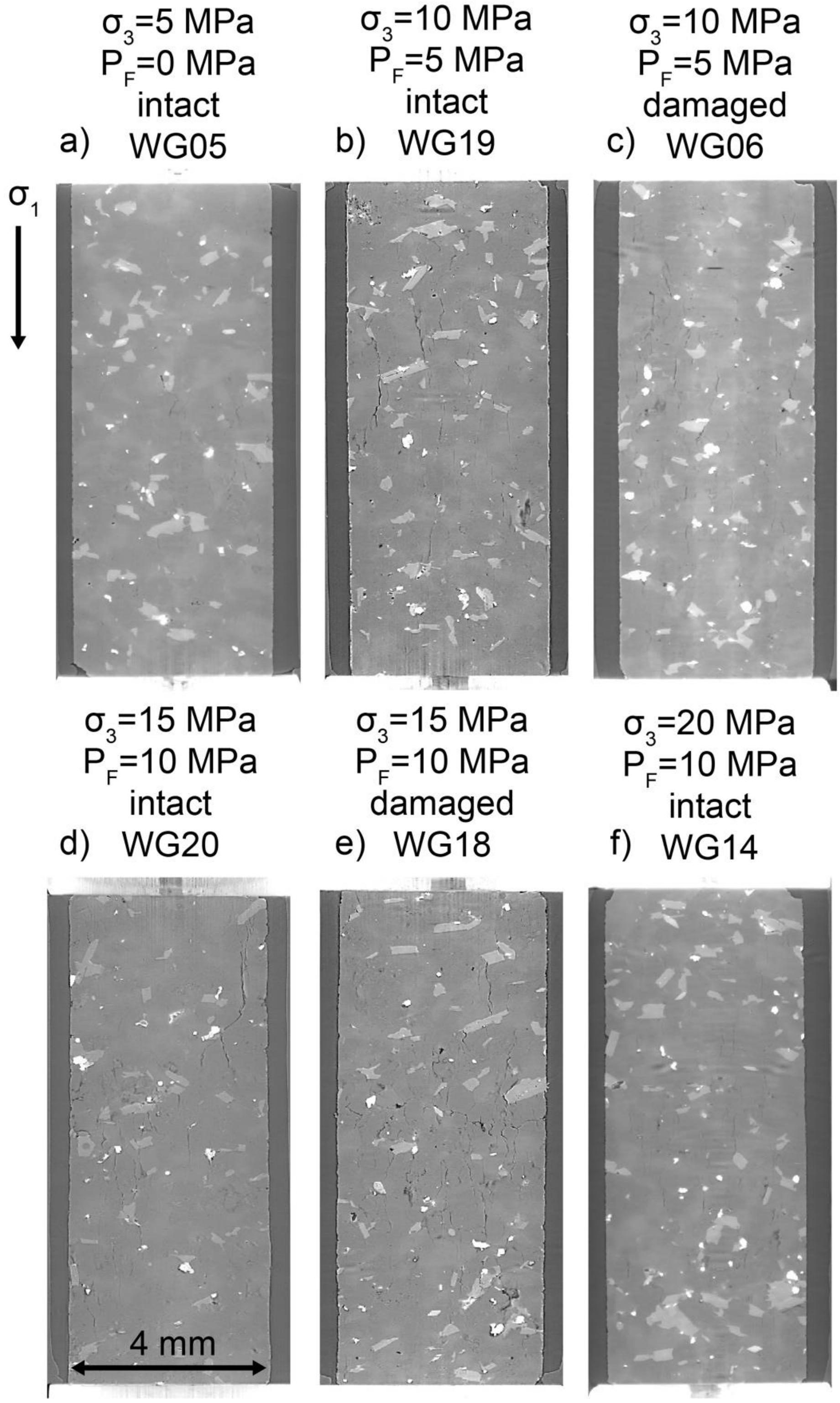

Figure 1. Two-dimensional slices of the tomograms acquired immediately preceding macroscopic failure in the six experiments. Minerals with larger densities, such as oxides and biotite, have larger gray-scale values in the tomograms (lighter gray and white regions), than minerals with lower densities, such as quartz and feldspar (darker gray). The fractures have

lower gray-scale values (dark gray and black). The applied confining pressure, σ_3, and fluid pressure, P_F, and whether the rock core was damaged or intact are listed above each slice.

2.2. Digital volume correlation analysis

To calculate the local three-dimensional strain fields, we used the software TomoWarp2 (Tudisco et al., 2017). Digital volume correlation analyses search for similar patterns of voxels in pairs of three-dimensional images and then calculate the displacement vector that maps a pattern in one image to a pattern in another image (e.g., Charalampidou et al., 2011). In TomoWarp2, the node spacing and correlation window size determine the spatial resolution and the size of the volume used to identify similar patterns of voxels, respectively. Calculations with a node spacing of 20 voxels (0.13 mm) and correlation window size of 10 voxels (65 µm) produce an acceptable spatial resolution and reasonable levels of signal to noise (McBeck et al., 2018). McBeck et al. (2018) examines the influence of several DVC parameters. Here, we use the same set of DVC parameters for all the experiments, and then we compare the degree of localization between the different experiments. Consequently, each DVC calculation has the same spatial resolution and amount of noise.

To identify the tomograms used in the digital volume correlation analysis, we divide each experiment into 20 equal increments of the macroscopic axial strain, ε_{zz}, and then identify the tomograms with the closest ε_{zz} to the specified increments (**Figure 2**), following our previous analyses (e.g., McBeck et al., 2018). There is a tradeoff between temporal resolution and noise in digital volume correlation analyses; in particular, a higher temporal resolution generally leads to more noise (McBeck et al., 2018). Here, we used 20 increments because it provides a good balance between temporal resolution (or macroscopic axial strain resolution) and amount of noise for these experiments. The optimal number of DVC calculations for a given experiment then depends on the tomogram quality, and amount of macroscopic axial strain that accumulates in the experiment.

We then use these pairs of tomograms to perform 19 digital volume correlation calculations for each experiment. TomoWarp2 reports three-dimensional fields of displacement vectors from which we calculate the nine components of the strain tensor. The resulting strain tensors are thus the local, incremental strains done between each tomogram acquisition, and not the total cumulative strain over the entire experiment. To quantify the localization of the volumetric and deviatoric components of the strain field, we calculate the divergence, $I1$, (volumetric strain, contractive, $I1 < 0$, and dilative, $I1 > 0$) and the second invariant of the deviatoric strain tensor, $J2$, (deviatoric strain, shear) from the incremental displacement fields. In previous analyses, we used the curl of the displacement field to characterize the shear strain, following the technique of the geodetic community (McBeck et al., 2019, 2020c). However, recent machine learning analyses suggest that $J2$ may provide more information about the timing of fault reactivation and macroscopic failure in strike-slip fault systems than the curl of the displacement field (McBeck et al 2022a). We also use $J2$ to characterize the shear strain because it determines the maximum distortion criterion, or von Mises yield criterion. Because each tomogram captures regions outside the rock core, such as the jacket and deformation apparatus, we remove the portion of the calculated strain field that is outside the rock core.

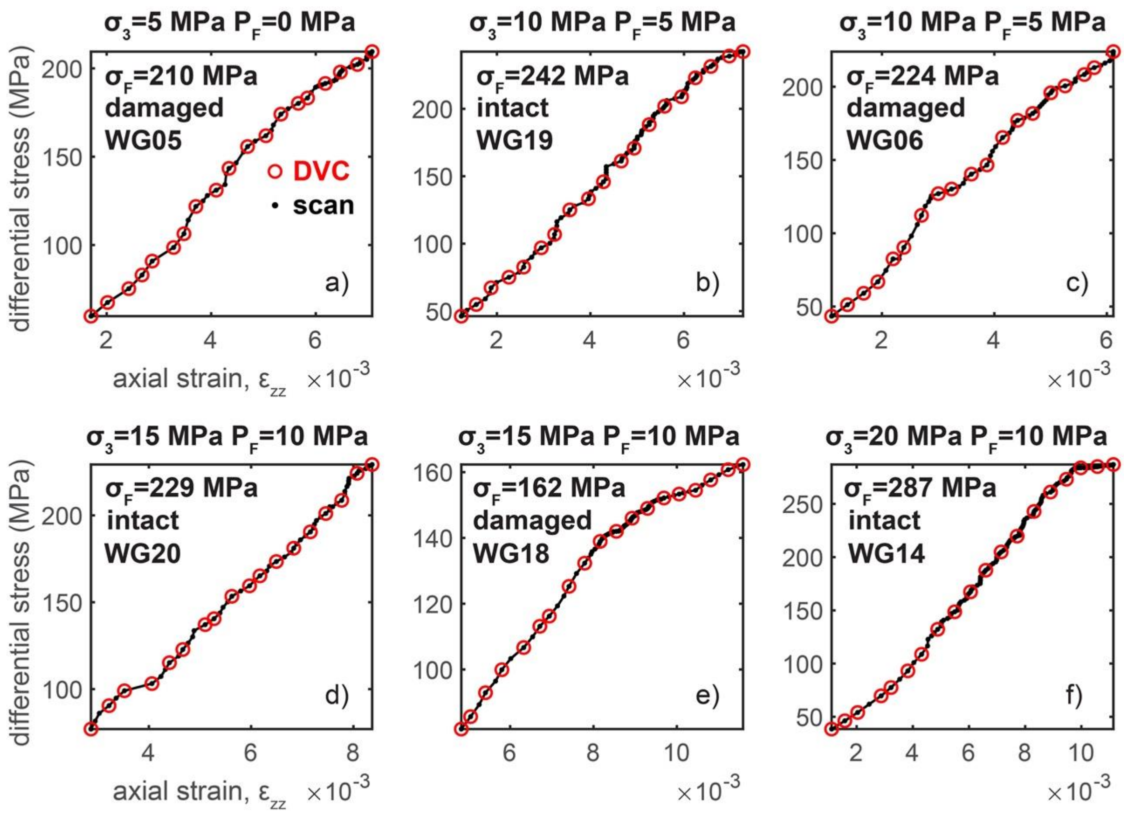

Figure 2. Differential stress and cumulative axial strain, ε_{zz}, when each tomogram or scan was acquired (black symbols) and the conditions of the scans used in the digital volume correlation (DVC) analyses (red symbols) for each experiment. The applied confining pressure, σ_3, fluid pressure, P_F, whether the core was heat-treated (damaged) before the experiment or not (intact), and the resulting maximum differential stress or failure stress, σ_F, are listed in each plot. The differential stress and ε_{zz} of the first scans shown here are not zero because we do not show the scans that were acquired during the early phase of each experiment when the axial strain-differential stress curve is highly non-linear and concave upward. This non-linearity is caused in part by the closure of preexisting fractures and pores, and to a larger extent by the settling of the rock core inside the apparatus as it comes in contact with the upper and lower pistons. We only include the scans following this non-linear stage in the digital volume correlation analysis.

3 Results

3.1. Evolution of the spatial localization of the strain components

To quantify the spatial localization of the contraction, $|I1 < 0|$, dilation, $I1 > 0$, and shear strain, $J2$, we compare the volume of the polyhedron that surrounds high values of each strain component, v_h, to the volume of the polyhedron that surrounds all of the values of the given strain component, v_t. For the shear strain, v_t is equal to the volume of the rock core used in the digital volume correlation analysis. For the volumetric strain components, v_t may be smaller than the volume of the rock core because the fraction of the rock core occupied by the dilation or contraction evolves throughout the experiment. Consequently, we first examine the evolution of this volume, v_t, divided by the volume of the total rock used in the digital volume correlation analysis for the dilation and contraction throughout each experiment. This comparison also provides insight into the influence of confining pressure, σ_3, on volumetric strain.

We report the time in the experiments using the normalized cumulative macroscopic axial strain, $\widetilde{\varepsilon_{zz}}$, measured from the change in height of the rock cores observed in the tomograms. We normalize the macroscopic axial strain so that the maximum and minimum values are one and zero. In particular, $\widetilde{\varepsilon_{zz}}$ is calculated from the ε_{zz} calculated for the given tomogram, the ε_{zz} of the tomogram acquired immediately preceding macroscopic failure, ε_{zz}^F, and the ε_{zz} of the first tomogram acquired at the onset of the linear phase early in loading, ε_{zz}^0, as $\widetilde{\varepsilon_{zz}} = (\varepsilon_{zz} - \varepsilon_{zz}^0)/(\varepsilon_{zz}^F - \varepsilon_{zz}^0)$.

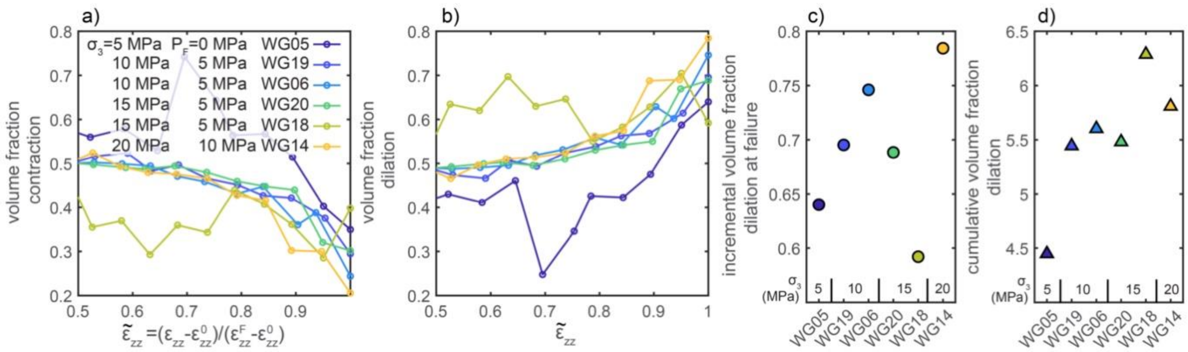

Figure 3. Fraction of the volume of the rock occupied by contraction, $I1 < 0$ (a) and dilation, $I1 > 0$ (b) as a function of the normalized cumulative macroscopic axial strain, $\widetilde{\varepsilon_{zz}}$, of the second tomogram used in each digital volume correlation calculation, and the incremental (c) and sum of the incremental, or cumulative, fraction occupied by dilation (d) at the end of each experiment. The normalized cumulative macroscopic axial strain, $\widetilde{\varepsilon_{zz}}$, is a function of the ε_{zz} calculated from the given tomogram, the ε_{zz} of the tomogram acquired immediately preceding macroscopic failure, ε_{zz}^F, and the ε_{zz} of the first tomogram acquired at the onset of the linear phase early in loading, ε_{zz}^0, as $\widetilde{\varepsilon_{zz}} = (\varepsilon_{zz} - \varepsilon_{zz}^0)/(\varepsilon_{zz}^F - \varepsilon_{zz}^0)$. The colors of the symbols indicate different experiments.

The volume fraction occupied by contraction generally decreases while the fraction occupied by dilation generally increases after about 0.8 $\widetilde{\varepsilon_{zz}}$ (**Figure 3**). The exception to this trend is experiment WG18. This experiment hosts relatively large volume fractions of dilation, up to 0.7, early in loading, when $\widetilde{\varepsilon_{zz}}$ is about 0.6. This experiment may have unique behavior because as this rock core was loaded into the deformation apparatus, it developed a core-spanning fracture perpendicular to the maximum compressive stress (**Figure S1**). Increasing axial stress during the experiment then closed the fracture.

To assess the influence of σ_3 on the volumetric strains, we compare the incremental volume fraction occupied by dilation immediately preceding failure, derived from the final digital volume correlation calculation, and the sum of the incremental (cumulative) volume fraction from the onset of loading to the end of the experiment. Both the incremental and cumulative strains indicate that larger σ_3 promotes dilation (**Figure 3c, d**). Experiment WG14, with the largest confining pressure (σ_3=20 MPa) and largest effective pressure (P_e=10 MPa), achieves the largest incremental volume fraction occupied by dilation at the end of the experiment, and immediately preceding failure (**Figure 3c**), and the second largest cumulative volume fraction (**Figure 3d**). Experiment WG05, with the smallest σ_3 (5 MPa), and smallest P_e (5 MPa), achieves the smallest cumulative and second smallest incremental volume fraction occupied by dilation at the end of the experiment. Experiment WG18, with σ_3=15 MPa and P_e=5 MPa, experiences the smallest incremental volume fraction and largest cumulative volume fraction occupied by dilation. The development of the core-spanning fracture produced a relatively high volume fraction of dilation earlier in loading in this experiment compared to the other experiments. In general, greater σ_3 and P_e promote dilation.

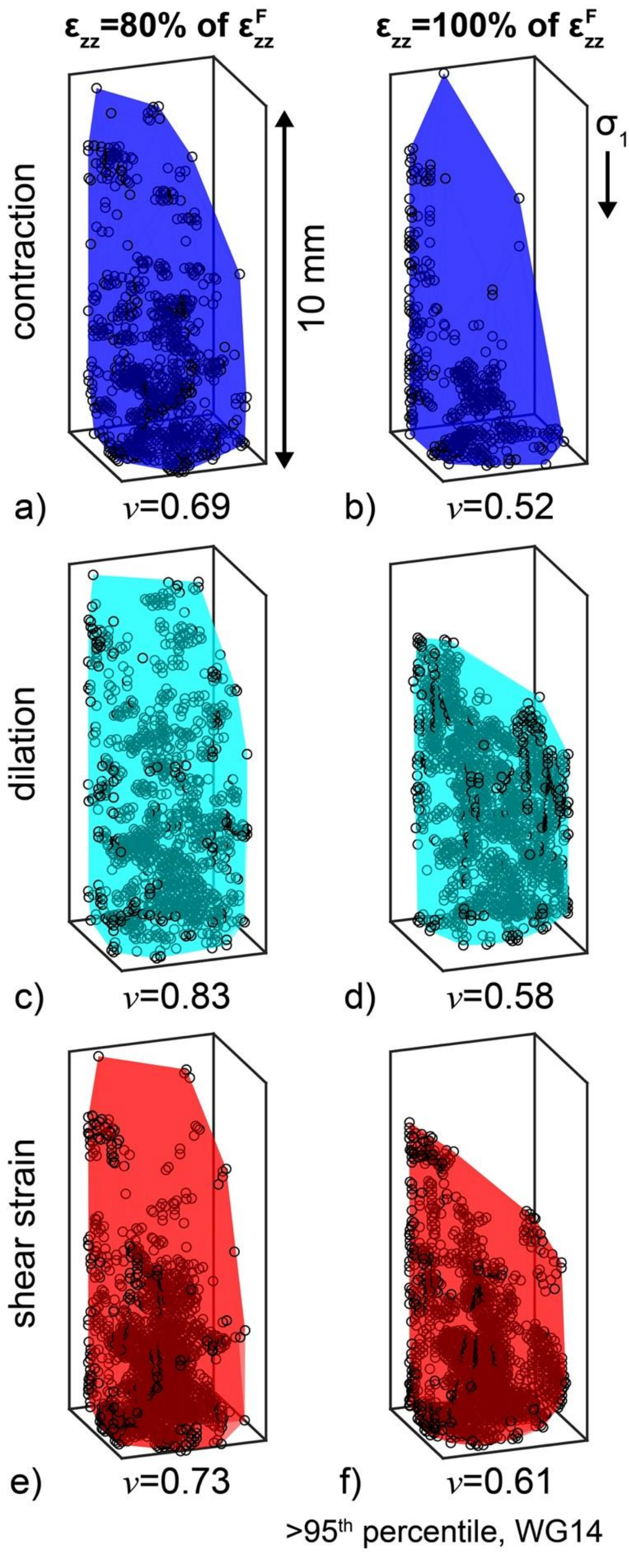

Figure 4. Spatial distribution of the high values (>95th percentile) of the contraction (a, b), dilation (c, d) and shear strain (e, f) at $\varepsilon_{zz}/\varepsilon_{zz}^F$=0.80 (a, c, e), and at $\varepsilon_{zz}/\varepsilon_{zz}^F$=1, immediately preceding macroscopic failure (b, d, f) for experiment WG14. Black circles show the location of the three-dimensional strain field with high values of incremental strain, >95th percentile. Shaded dark blue, light blue and red areas show the convex hull that fits around the high strain values. The numbers below each plot show the fraction of the volume of the convex hull relative to the total volume occupied by all of the values of the strain component, v. The v of the contraction, dilation, and shear strain all decrease with increasing differential stress, from 80% to 100% of ε_{zz}^F.

As described above, we calculate the volume of the convex hull or polyhedron that surrounds the population of the high strains, v_h, for each of the 19 digital volume correlation calculations performed in each experiment in order to quantify the spatial localization of the high strain values. We select the high strain values using a range of thresholds defined by the percentiles of the strain population at a given stress step, which we describe in more detail below. We find the polyhedron that surrounds the high strains using a Matlab function that identifies a convex hull around a set of points in three-dimensions (*convhull*). We use this metric, rather than a previous metric we used to quantify the localization of strain (McBeck et al., 2022b), because this metric does not require defining a grid size, and thus the results are independent of this parameter. We report v_h divided by the volume of the polyhedron that surrounds all of the values of the given strain component, v_t, as $v = v_h/v_t$. **Figure 4** shows the polyhedrons and resulting v found for the contractive, dilative, and shear strain values greater than the 95th percentile value at two different time steps (and digital volume correlation calculations) in experiment WG14. One of the time steps occurs immediately preceding macroscopic failure, when the ε_{zz} of the second tomogram used in the digital volume correlation analysis is equal to the ε_{zz} of the final tomogram acquired in the experiment, ε_{zz}^F, or $\varepsilon_{zz}/\varepsilon_{zz}^F = 1$. The other time step is earlier in the experiment, when $\varepsilon_{zz}/\varepsilon_{zz}^F = 0.8$. These example polyhedrons show that the v of each strain component decreases with increasing differential stress and cumulative axial strain, indicative of localization towards macroscopic failure.

Figure 5 shows v for each strain component and all of the experiments for two of the percentile thresholds used to identify the high strain values, the 50th and 90th percentile. We perform the analyses with six different thresholds (50th, 60th, 70th, 80th, 90th, 95th), and summarize those results in subsequent sections. When the dilation or contraction are greater than the 50th or 90th percentile, all but one or two experiments (other than experiments WG05 and WG18) host decreases in v after about 0.8 to 0.9 $\widetilde{\varepsilon_{zz}}$. For the shear strain, a smaller number of the experiments host decreases in v toward failure. The decreasing v indicates that the high strain events localize. We next quantify these decreases in v approaching macroscopic failure.

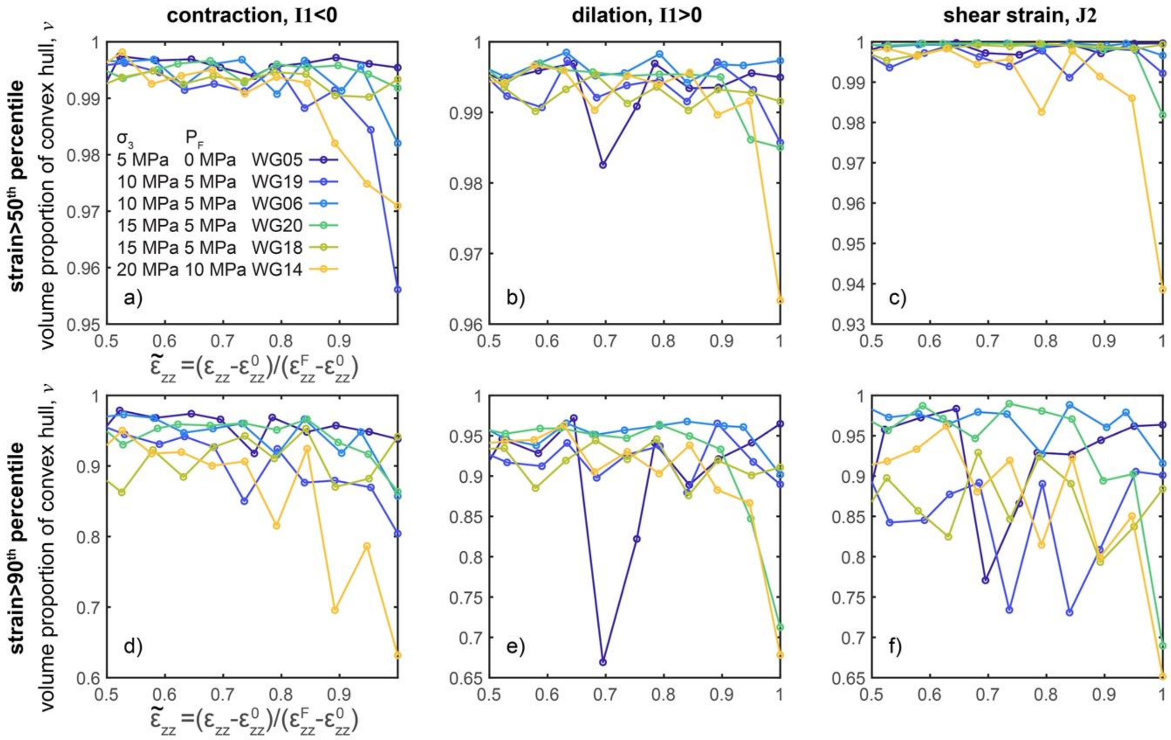

Figure 5. Evolution of the volume fraction of the convex hull around the high strain values, v, for strains greater than the 50th percentile (a-c) and 90th percentile (d-f), for the absolute value of the contraction, $|I1 < 0|$, (a, d) dilation, $I1 > 0$, (b-e) and shear strain, $J2$ (c, f). The different colors of the curves correspond to the different experiments.

To quantify the evolution of v, we first examine the cumulative localization approaching macroscopic failure. **Figure 6** shows the absolute value of the sum of the negative values of the change in v from one digital volume correlation calculation to the next, when $\widetilde{\varepsilon_{zz}}$>0.5, $\sum_{\widetilde{\varepsilon_{zz}}=0.5}^{\widetilde{\varepsilon_{zz}}=1} |\Delta v(\Delta v < 0)|$. Negative Δv indicates that the volume of the polyhedron that surrounds the high strain events decreases from one digital volume correlation calculation to the next, and thus the high strain events localize from one stress step to the next. We sum the values when $\widetilde{\varepsilon_{zz}}$>0.5, and not from the onset of loading, because we aim to characterize strain localization approaching macroscopic failure. Larger values of the cumulative localization thus indicate greater magnitudes of localization toward macroscopic failure.

The cumulative localization increases with the strain threshold (**Figure 6**). The analysis thus detects more localization with larger strain thresholds. This trend is expected because larger strain thresholds produce lower numbers of high strain events. The cumulative localization increases with σ_3 for the contraction, dilation, and shear strain for all of the thresholds <95th percentile (**Figure 6g-i**). When the threshold is the 95th percentile, the cumulative localization increases with σ_3 for the contraction and shear strain, but not the dilation (**Figure 6h**). Dividing the experiments into groups with relatively lower and higher σ_3 helps show that the cumulative localization increases with σ_3 (**Figure 6d-f**). Using all of the thresholds, the mean of the cumulative localization of the contraction for the experiments with σ_3>10 MPa is 36% greater than the mean of the experiments with $\sigma_3 \leq$10 MPa. This difference is 13% and 41% for the dilation and shear strain, respectively. The generally positive slopes of the lines that fit through the cumulative localization and σ_3 for each strain component and each threshold also indicate that larger σ_3 produces greater cumulative localization.

The results reveal differences in the cumulative localization of the nominally intact rocks and heat-treated, damaged rocks (**Figure 6d-f**). The intact rocks tend to experience more cumulative localization than the damaged rocks. In particular, the mean of the cumulative localization of the intact rocks is 38%, 25%, and 50% greater than the mean of the damaged rocks for the contraction, dilation, and shear strain, respectively.

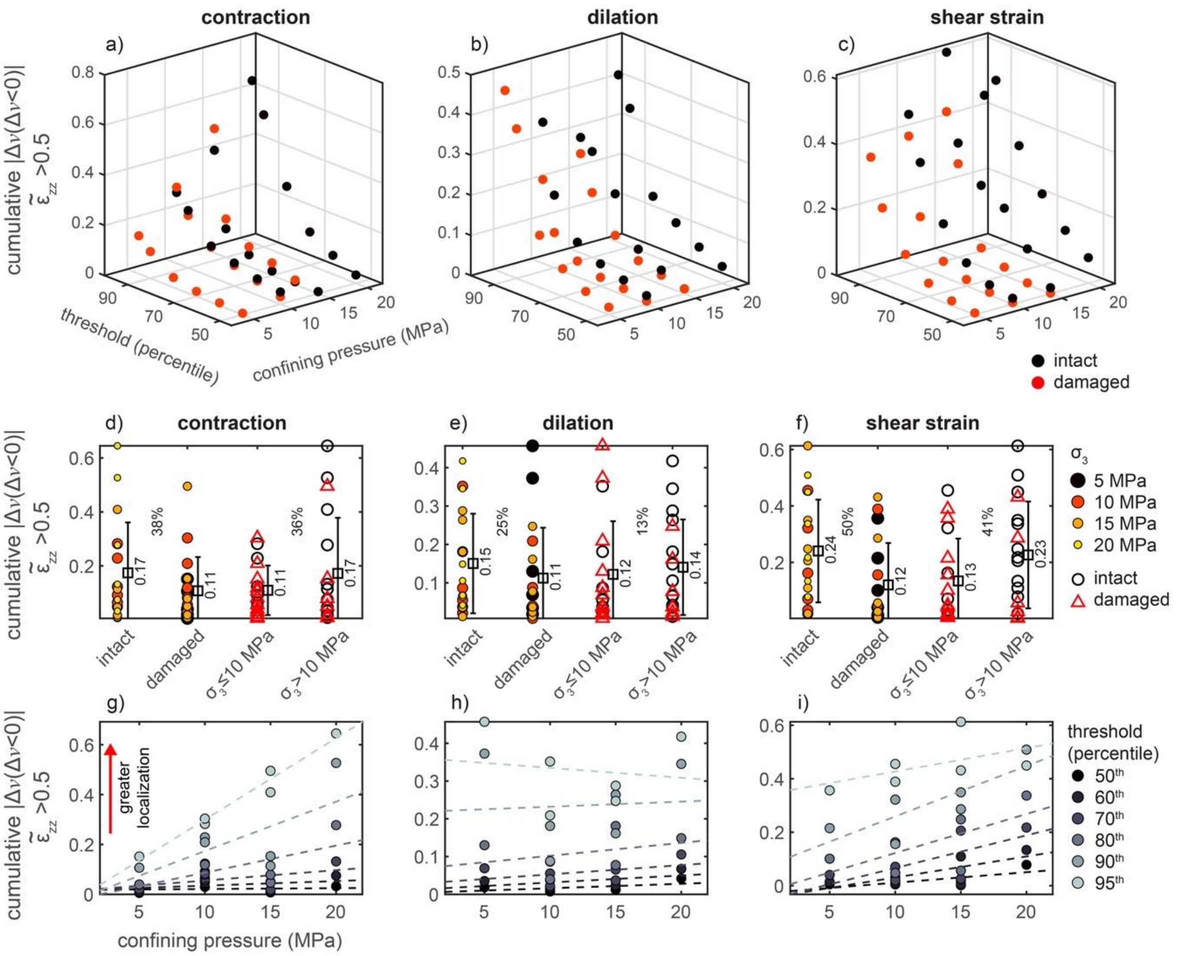

Figure 6. The cumulative localization hosted by each strain component approaching failure, calculated as the sum of the absolute value of the negative change in v when $\widetilde{\varepsilon_{zz}}>0.5$, $\sum_{\widetilde{\varepsilon_{zz}}=0.5}^{\widetilde{\varepsilon_{zz}}=1}|\Delta v(\Delta v<0)|$. Negative Δv indicates that the volume of the polyhedron that surrounds the high strain events decreases from one digital volume correlation calculation to the next, and thus the high strain events localize from one stress step to the next. The top row (a-c) shows three-dimensional plots of the cumulative localization as a function of the applied confining pressure, σ_3, and the thresholds used to identify the high strains for the contraction (a), dilation (b), and shear strain (c). The black and red symbols indicate if the sample was intact (black) or damaged (red). The second row (d-f) shows the cumulative localization grouped by the intact and damaged rocks, and experiments with lower σ_3 (≤10 MPa) and higher σ_3 (>10 MPa). The color and size of the symbols indicate the σ_3 for the grouping of the intact and damaged rocks. The black circles and red triangles indicate if the sample was intact (black) or damaged (red) for the grouping of the lower and higher σ_3. The square symbols and error bars show the mean ± one standard deviation of each group of data points. The number next to each error bar lists the mean. The percentages between each pair of

groups shows the percentage difference between the magnitude of the larger mean, μ_{max}, and smaller mean, μ_{min}, as $(\mu_{max} - \mu_{min})/\mu_{max}$. The third row (g-i) shows the cumulative localization as a function of σ_3. The color of the symbols indicates the threshold used to identify the high strain values. The dashed lines show the fit of the linear function through the data derived from each threshold. The intact rocks localize by larger amounts than the damaged rocks. Experiments with larger confining pressure generally host more localization than experiments with lower confining pressure.

We also examine alternative methods of quantifying the evolution of v approaching macroscopic failure, in addition to the cumulative localization (**Figure 6**). **Figure 7** shows the localization preceding macroscopic failure measured using the difference in v from the final tomogram acquired immediately preceding failure, when $\widetilde{\varepsilon_{zz}}$ is one, and when $\widetilde{\varepsilon_{zz}}$ is 0.8, Δv. Negative Δv indicates that the high strain events localize towards macroscopic failure. **Figure S2** and **Figure S3** show the Δv calculated using $\widetilde{\varepsilon_{zz}}$ of 0.5 and using $\widetilde{\varepsilon_{zz}}$ of 0.9, which produce similar results to those reported for when $\widetilde{\varepsilon_{zz}}$ is 0.8.

Using all of the tested combinations of strain components, experiments, high strain thresholds, and selected $\widetilde{\varepsilon_{zz}}$, Δv is negative in 75% of the tested combinations. This high rate indicates that the vast majority of strain components localize toward failure. However, this rate varies among the different strain components. For the dilation and contraction, Δv is negative in 80% of the tested combinations. For the shear strain, in contrast, Δv is negative in only 67% of the tested combinations. Consequently, the volumetric strain components are more likely to experience localization approaching macroscopic failure than the shear strain.

The trends observed in this localization metric (**Figure 7**, **Figure S2**, **Figure S3**) are similar to those observed for the cumulative localization (**Figure 6**). The amount of localization increases with the high strain threshold and σ_3, producing increasingly negative Δv (**Figure 7g-i**). Consequently, the experiments with higher σ_3 localize more than the experiments with lower σ_3. In addition, the intact rocks localize more than the damaged rocks. The trends observed here also occur when we calculate Δv using $\widetilde{\varepsilon_{zz}}$=0.5, and $\widetilde{\varepsilon_{zz}}$=0.9 (**Figure S2**, **Figure S3**), and for the v observed in the final digital volume correlation calculation, which captures the strain field immediately preceding macroscopic failure (**Figure S4**).

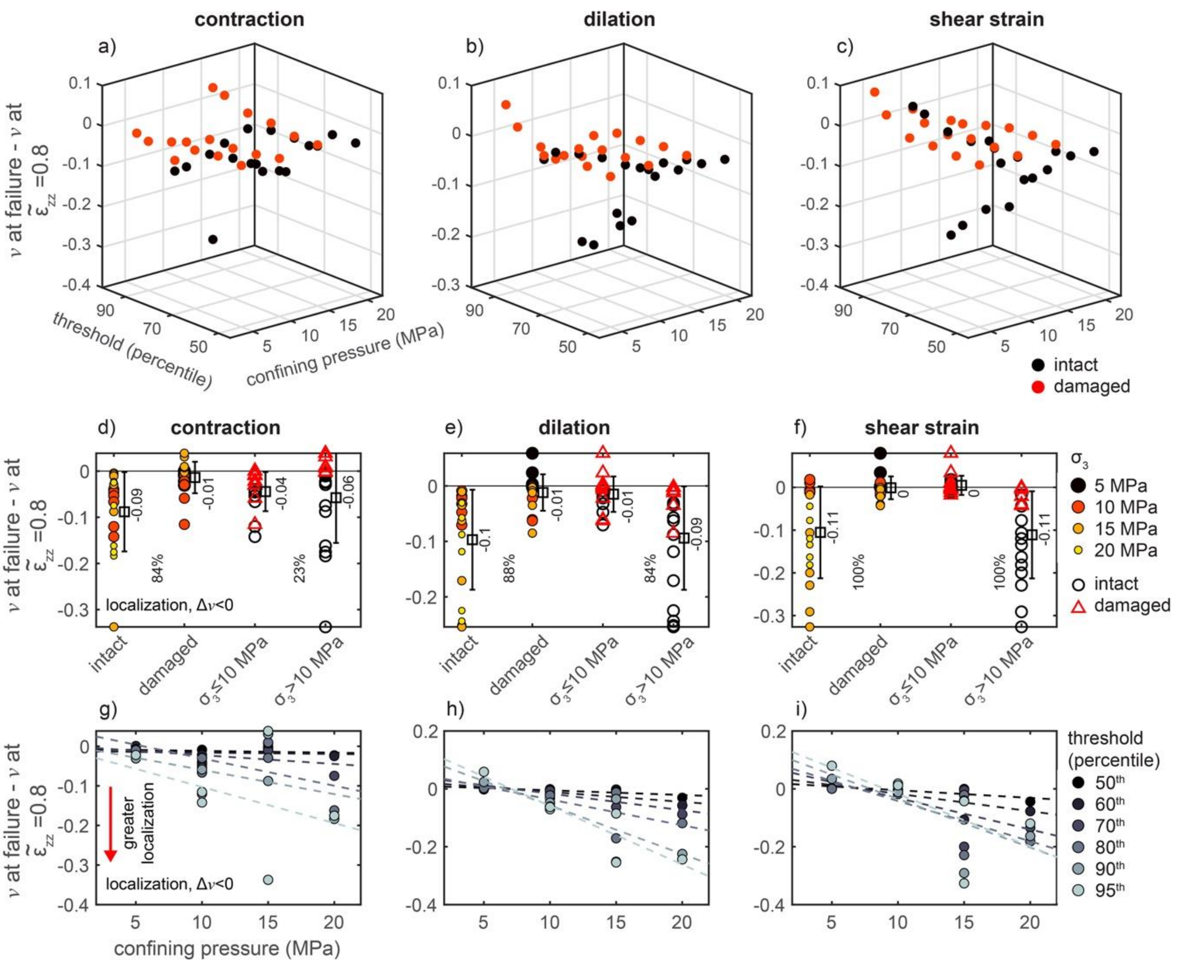

Figure 7. Localization immediately preceding failure measured as the difference in v from the final tomogram acquired immediately preceding failure, when $\widetilde{\varepsilon_{zz}}$ is one, and when $\widetilde{\varepsilon_{zz}}$ is 0.8, Δv. Negative Δv indicates that the high strain events localize towards macroscopic failure. The format of the figure is the same as **Figure 6**. The intact rocks experience larger amounts of localization preceding macroscopic failure, more negative Δv, than the damaged rocks. The experiments with larger confining pressure host more localization than experiments with lower confining pressure.

To compare the influence of σ_3 on localization, we now report the slope of the line that fits σ_3 and 1) Δv from $\widetilde{\varepsilon_{zz}}$=0.5, 0.8 or 0.9 to macroscopic failure, 2) the cumulative localization, and 3) v at the end of each experiment (**Figure 8**). These slopes approximate the influence of σ_3 on localization near failure for each strain component. **Figure 6**, **Figure 7**, and **Figures S2-S4** show these lines. **Figure S5** shows the slopes derived from all the strain thresholds, and **Figure 8** shows the slopes derived using a threshold of the 90th percentile. Higher percentile thresholds produce larger slopes (**Figure S5**), and so we focus on one percentile here in order to highlight the trends observed for the other percentiles.

For each of the localization metrics except the cumulative localization, the dilation and shear strain produce larger negative slopes than the contraction (**Figure 8**). This result indicates that σ_3 has a stronger influence on the amount of localization near failure for the dilation and shear strain than the contraction. For the cumulative localization, the slopes of the shear strain and contraction are more negative than the slope of the dilation, indicating that σ_3 has a weaker influence on the amount of cumulative localization approaching failure for the dilation than the shear strain or contraction. The relative magnitudes of the slopes of the cumulative localization may differ from the slopes of the other metrics because the cumulative localization of the experiment WG05, with the lowest σ_3, is similar to the cumulative localization of the experiments with higher σ_3. The large and sudden decrease in v for the dilation at $\widetilde{\varepsilon_{zz}}$ of 0.7 produces large cumulative localization for experiment WG05 relative to the other experiments with lower σ_3 (**Figure 5**). This temporary decrease in v, however, does not produce similarly anomalous values of Δv calculated using $\widetilde{\varepsilon_{zz}}$ of 0.5, 0.8 and 0.9, or the v at macroscopic failure. Consequently, the other localization metrics are not influenced by this temporary decrease, and in general, σ_3 has a larger influence on the dilation and shear strain than the contraction.

This result agrees with previous analyses that highlight the close correlation between dilation and shear during rock deformation and fault development (Moore & Lockner, 1995; McBeck et al., 2020c). Because fracture surfaces are initially rough, they must open, or dilate, before sliding and shear may occur on them. Consequently, we expect similarities in the accumulation and localization of the dilative and shear strain. In agreement with these expectations, σ_3 has a larger influence on the dilation and shear strain than the contraction in these experiments.

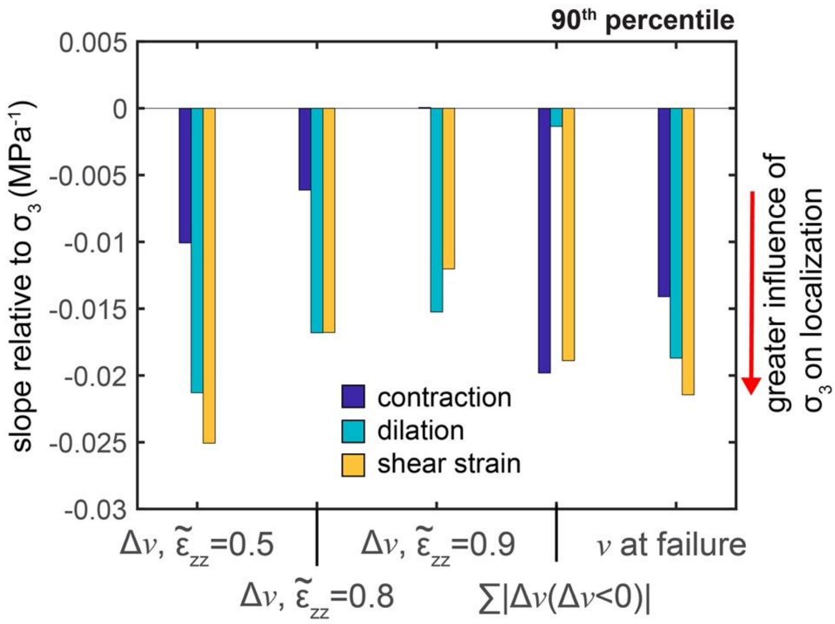

Figure 8. Slopes of the linear fit of different localization metrics for strains >90th percentile and σ_3 of the experiments for each strain component: contraction (dark blue), dilation (light blue), and shear strain (yellow). The horizontal axis indicates the localization metrics: 1-3) Δv using $\widetilde{\varepsilon_{zz}}$=0.5, $\widetilde{\varepsilon_{zz}}$=0.8, and $\widetilde{\varepsilon_{zz}}$=0.9, 4) the cumulative localization, and 5) v at failure. The slopes derived from the cumulative localization were multiplied by negative one so that larger negative values indicate a stronger influence of σ_3 on localization for all the metrics. The lines that produce each slope are shown in **Figure 6**, **Figure 7**, **Figure S2**, **Figure S3**, and **Figure S4**. In all but one of the localization metrics, the σ_3 has a larger influence on the dilation and shear strain than the contraction.

3.2. Phases of delocalization and localization

The previous section focuses on the change in localization preceding macroscopic failure. Here, we compare the proportion of the experiment time, in terms of $\widetilde{\varepsilon_{zz}}$, that each strain component is localizing, and the timing of when the maximum localization occurs relative to macroscopic failure. In an ideal system that lacks significant heterogeneities, one may expect that the high strain values would continually localize with increasing axial strain or differential stress (Lyakhovsky et al., 2011). Consequently, the proportion of $\widetilde{\varepsilon_{zz}}$ in which the Δv from one digital volume correlation calculation to the next is less than zero should be one. However, for all of the tested strain thresholds, strain components, and experiments, this proportion is always less than one, indicating that the high strains experience temporary episodes of delocalization (**Figure 9**). The intact rocks tend to experience localization for a longer proportion of $\widetilde{\varepsilon_{zz}}$ than the damaged rocks (**Figure 9d-f**). On average, the intact rocks experience localization for 13% (contraction), 23% (dilation), and 16% (shear strain) more $\widetilde{\varepsilon_{zz}}$ than the damaged rocks. Thus, the damaged rocks have longer total phases of delocalization than the intact rocks.

For the dilation and shear strain, the experiments with higher σ_3 tend to host localization for a longer period of $\widetilde{\varepsilon_{zz}}$ than the experiments with lower σ_3. The experiments with σ_3 >10 MPa host localization on average for 24% (dilation) and 25% (shear) more $\widetilde{\varepsilon_{zz}}$ than the experiments with σ_3 ≤10 MPa (**Figure 9f**). For the contraction, the experiments with σ_3 ≤10 MPa host slightly longer periods of $\widetilde{\varepsilon_{zz}}$ with localization (8%) than the experiments with 3 >10 MPa.

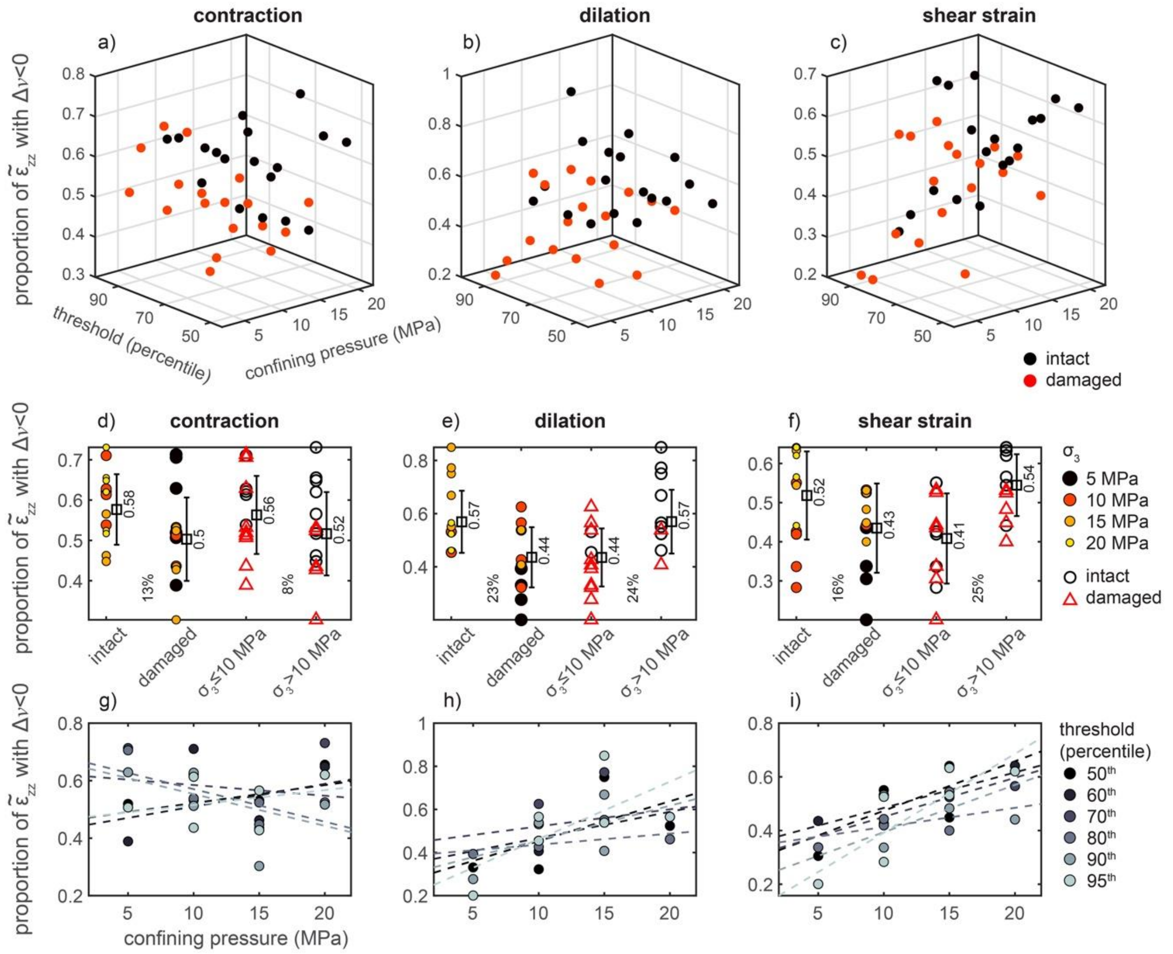

Figure 9. Proportion of the experiment time, in terms of $\widetilde{\varepsilon_{zz}}$, in which the strain component

produces negative Δv, and thus localizes. Format is the same as **Figure 6**. The intact rocks experience larger proportions of $\widetilde{\varepsilon_{zz}}$ in which the strain components localize than the damaged rocks. The experiments with larger confining pressure generally host more $\widetilde{\varepsilon_{zz}}$ in which the strain components localize.

These results indicate that the high strain values do not systematically increase in localization with increasing differential stress or axial strain. Instead, they experience episodes of delocalization, rather than a continuous increase or acceleration of localization toward catastrophic failure. **Figure 10** shows the $\widetilde{\varepsilon_{zz}}$ when each strain component experiences its minimum v, and thus maximum localization. The damaged rocks host their maximum localization earlier in loading than the intact rocks (**Figure 10d-f**). The maximum localization occurs on average at $\widetilde{\varepsilon_{zz}}$ of 0.86, 0.72, and 0.79 for the contraction, dilation and shear strain, respectively, of the damaged rocks. In contrast, for the intact rocks, the maximum localization occurs on average at $\widetilde{\varepsilon_{zz}}$ of 1, 0.98, and 0.93 for the contraction, dilation and shear strain, respectively. The differences in σ_3 produce only small differences in the timing of the maximum localization.

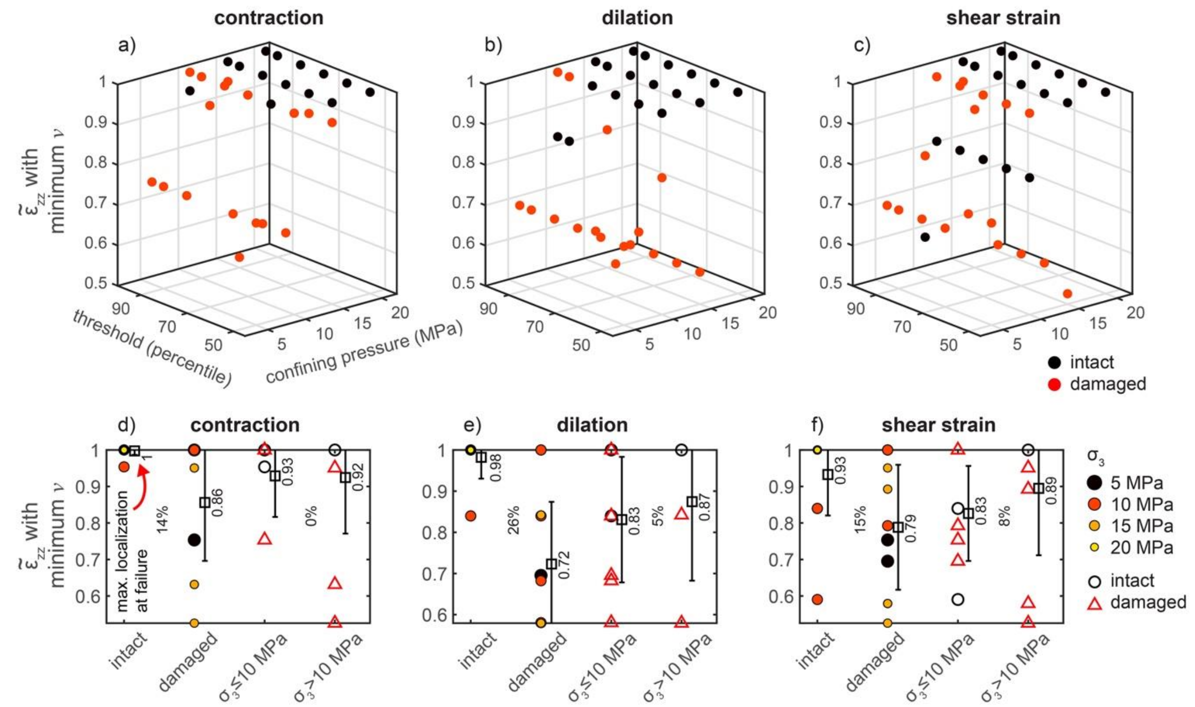

Figure 10. Timing of the maximum localization, minimum v, in terms of $\widetilde{\varepsilon_{zz}}$. Format is the same as **Figure 6** (a-f). The intact rocks tend to host their maximum localization immediately preceding failure, when $\widetilde{\varepsilon_{zz}}$ is one. In contrast, the damaged rocks host their maximum localization earlier in loading.

4 Discussion

4.1. The influence of confining pressure on volumetric strain

Tracking the volume of the rock occupied by dilation in the experiments on damaged and intact rocks, at confining pressures of 5-20 MPa, and effective pressures of 5 MPa and 10 MPa indicates that the volume of rock that experiences dilation generally increases toward failure, particularly after about 0.8 $\widetilde{\varepsilon_{zz}}$ (**Figure 3**). This evolution is consistent with previous digital volume correlation analyses of X-ray tomogram triaxial compression experiments (Renard et al., 2019, McBeck et al., 2019, 2020c). The observed increase of the local, incremental dilation with increasing differential stress is also consistent with previous measurements of the macroscopic, cumulative volumetric strain of Westerly granite during triaxial compression (e.g., Brace et al., 1966, Bieniawski, 1967; Brace, 1978). In triaxial compression experiments on low porosity crystalline rocks, the macroscopic volumetric strain measured from the change in shape of the sample first evolves with the differential stress approximately linearly, with increasingly contractive values, or negative in the adopted sign convention. Then, at the onset of dilatancy, C', which may be about 50-75% of the stress at failure (Brace, 1978), the volumetric strain begins to develop increasingly dilative values, and the macroscopic dilation continually increases until macroscopic failure. The progressive increase of the macroscopic dilation observed following C' in previous triaxial compression experiments is consistent with the observed acceleration of the volume of rock occupied by dilation observed in the present analysis.

Comparing the fraction of the rock core that hosts dilation immediately preceding failure among the experiments indicates that increasing σ_3 generally promotes greater dilation (**Figure 3**). One may expect that greater σ_3 would suppress dilation. Indeed, triaxial compression experiments on porous rocks such as Berea sandstone and Adamswiller sandstone show that when σ_3 increases from 5 MPa to 40 MPa, the cumulative amount of inelastic dilation, which occurs following the onset of dilatancy and until macroscopic failure, decreases (Jamison & Teufel, 1979; Wong et al., 1997). However, for low porosity crystalline rocks, the relationship between σ_3 and the dilation follows the opposite trend observed in the sandstone (e.g., Brace & Orange, 1968; Crouch, 1970; Paterson & Wong, 2005 p. 70), and the same trend observed in the present experiments. In particular, for Westerly granite and Witwatersrand quartzite, larger σ_3 increases the inelastic dilation within the range of 3 to 30 MPa σ_2 for the quartzite, and 160 to 500 MPa σ_3 for the granite (Brace & Orange, 1968; Crouch, 1970). These results highlight a fundamental difference in the accumulation of dilatancy in low porosity crystalline rocks, in which fracture propagation and opening promotes dilatancy, and porous rocks, in which pore collapse and cataclasis may inhibit dilatancy.

To compare our results to this previous work, we calculate the amount of inelastic volumetric strain (dilation) that develops between the onset of dilatancy, C' (Brace, 1978), and macroscopic failure using the change in shape of the rock core observed in the X-ray tomograms (**Figure 11a, b**). We then compare these values to the sum of the volume fraction occupied by dilation, and the sum of the mean dilation from the onset of loading until failure calculated from the local incremental strains derived via digital volume correlation (**Figure 11c, d**). The identified values of C' are estimates based on the reversal in the slopes of the volumetric strain and differential stress curves. These estimates occur near 75% of the differential stress at failure, consistent with previous observations of the stress at C' (Brace, 1978).

Examining the macroscopic inelastic volumetric strain indicates that increasing σ_3 generally promotes more inelastic dilation (**Figure 11b**). The two damaged experiments, WG06 and WG18, deviate from the overall trend of increasing inelastic dilation with increasing σ_3. These experiments produce more inelastic strain than expected from the intact experiments with the corresponding σ_3. Previous work shows that more preexisting damage generally produces longer macroscopic yielding phases in which more volumetric and axial strain accumulate. In particular, sandstone with some significant porosity accumulates more volumetric and axial strain than granite during triaxial compression (e.g., Feng et al., 2019). Examining the cumulative volume fraction of dilation also shows that the damaged experiments WG06 and WG18 host larger volume fractions of dilation than expected from the corresponding intact experiments (**Figure 11c**). In summary, the cumulative volume fraction (**Figure 11c**), the cumulative mean dilation (**Figure 11d**), and the macroscopic inelastic volumetric strain (**Figure 11b**) all suggest that larger σ_3 promotes more dilation, consistent with previous measurements of low porosity crystalline rock (e.g., Brace & Orange, 1968; Crouch, 1970).

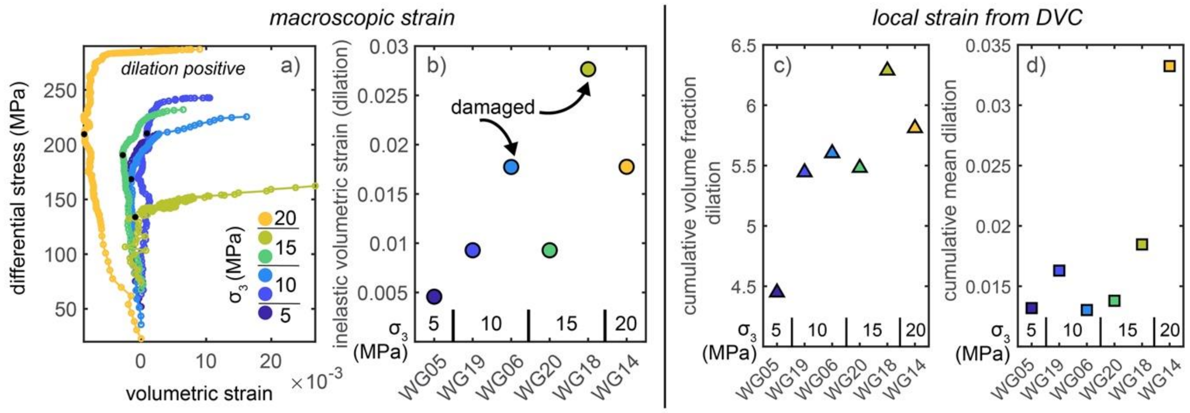

Figure 11. The influence of σ_3 on dilatancy. Evolution of the volumetric strain calculated from the shape change of the rock core observed in the X-ray tomograms (a), the amount of inelastic volumetric strain between the onset of dilatancy, C', and macroscopic failure (b), and the cumulative volume fraction of the dilation (c) and cumulative mean dilation (d) calculated from the local strain derived from digital volume correlation. The black dots in (a) shows the location of C'. Increasing σ_3 produces more dilation.

4.2. The influence of confining pressure on localization approaching macroscopic failure

Tracking the volume of the polyhedron that surrounds the high contraction, dilation and shear strain indicates that the high strain events localize approaching macroscopic failure in all three components for the vast majority of the experiments (**Figure 5**). This trend agrees with experimental observations of acoustic emissions that localize following the peak differential stress in triaxial compression experiments on granite, as the fractures coalesce into a system-spanning shear fracture (Lockner et al., 1991). Here, we identify localization of strain events preceding the peak differential stress, or failure stress. For all the tested parameters, the dilation localizes approaching failure more often (80% of the combinations of parameters produce negative changes in volume) than the shear strain (67%) (e.g., **Figure 6**, **Figure 7**). This result is consistent with a previous analysis of the localization of the volumetric and shear strain in a different set of X-ray tomography experiments on Westerly granite, Fontainebleau sandstone, Mt. Etna basalt, Green River shale, and Anstrude limestone (McBeck et al., 2022b). In this previous analysis and the present analysis, the high magnitudes of the volumetric strains localize to a greater extent than the shear strain. In addition, in the present analysis, the maximum strain localization occurs immediately preceding failure for the dilation, on average at 0.98 $\widetilde{\varepsilon_{zz}}$ for the intact rocks, but occurs earlier in loading for the shear strain, on average at 0.93 $\widetilde{\varepsilon_{zz}}$ for the intact rocks (**Figure 10**). Thus, the dilation hosts more systematic increases in localization towards failure than the shear strain, and the timing of maximum localization occurs almost exactly at macroscopic failure. Consequently, both the previous and present analyses suggest that the high magnitudes of the volumetric strains may provide more reliable information about the timing of catastrophic failure than the shear strain. Indeed, machine learning analyses indicate that the evolution of the dilative strain helps predict the timing of macroscopic failure in X-ray tomography experiments, and that the shear strain provides less useful information about the timing of failure (McBeck et al., 2020a). However, machine learning analyses of three-dimensional discrete element method numerical models of segmented fault networks within shear zones indicate that the shear strain provides more useful information about the timing of fault reactivation and macroscopic failure than the volumetric strain (McBeck et al., 2022a). Consequently, the utility of the volumetric strains for predicting the timing of failure may depend on the existence of system-spanning, macroscopic faults. In particular, in systems with macroscopic faults, shear strain may be a more reliable predictor of the timing failure than the dilative strain, as demonstrated by machine learning analyses on discrete element method models of shear zones that contain system-scale faults (McBeck et al., 2022a). In contrast, in systems that lack system-spanning preexisting faults, such as the rock cores in the triaxial compression experiments or healed faults in the crust, the dilative strain is a more reliable predictor of the timing of failure. This difference may occur because preexisting faults help localize shear strain, and allow it to accumulate in a systematic evolution.

Comparing the degree of localization near failure among the different experiments indicates that higher σ_3 promotes greater localization approaching macroscopic failure (**Figure 5**, **Figure 6**, **Figure 7**, **Figures S2-S5**). In the brittle portion of the crust, strike-slip faults tend to develop flower structures: a diffuse network of fractures near the surface that then localizes into a narrower zone at depth (Harding, 1985; Sylvester, 1988; Le Guerroue & Cobbold, 2006, Rockwell & Ben-Zion, 2007) (**Figure 12a**). This structure implies that increasing confining pressure promotes localization. In addition, seismic observations indicate that low velocity zones surrounding large crustal faults, such as the San Jacinto fault (Wang et al., 2019), can narrow with depth. Moreover, low magnitude seismicity between large magnitude earthquakes in southern and Baja California increases in localization with increasing depth (Ben-Zion & Zaliapin, 2019). Such fault zones are the result of the accumulation of many cycles of fault growth, including coseismic slip and precursory localization. Here, we show that in one cycle of precursory deformation leading to macroscopic failure, greater confining pressure leads to greater localization of the high strain events.

Observations of post-mortem fracture networks that form in uniaxial and triaxial compression experiments support the idea that increasing confining pressure promotes localization (e.g., Paterson, 1958; Paterson & Wong, 2005 p. 212; Rizzo et al., 2018). Under uniaxial compression and low confining pressures in triaxial compression, rock cores fail by axial splitting, in which arrays of fractures aligned parallel to the maximum compression direction develop (e.g., **Figure 12b**). These fracture networks are often diffusely distributed, with several fractures extending from the top to the bottom of the core (e.g., Akdag et al., 2021; Basu et al. 2013; Hu et al., 2021). Under higher confining pressures, the rock cores fail through the development of one or a few macroscopic shear fractures, perhaps as a pair as conjugate shear fractures (e.g., Paterson, 1958; Lee & Rathnaweera, 2016). Although these fractures may develop from the coalescence of many small fractures, the final fracture geometry identified following the maximum stress consists of a few system-spanning fractures. Consequently, the fracture geometries that develop under uniaxial compression and low confining pressure tend to be less localized than the fracture geometries that develop at higher confining pressures.

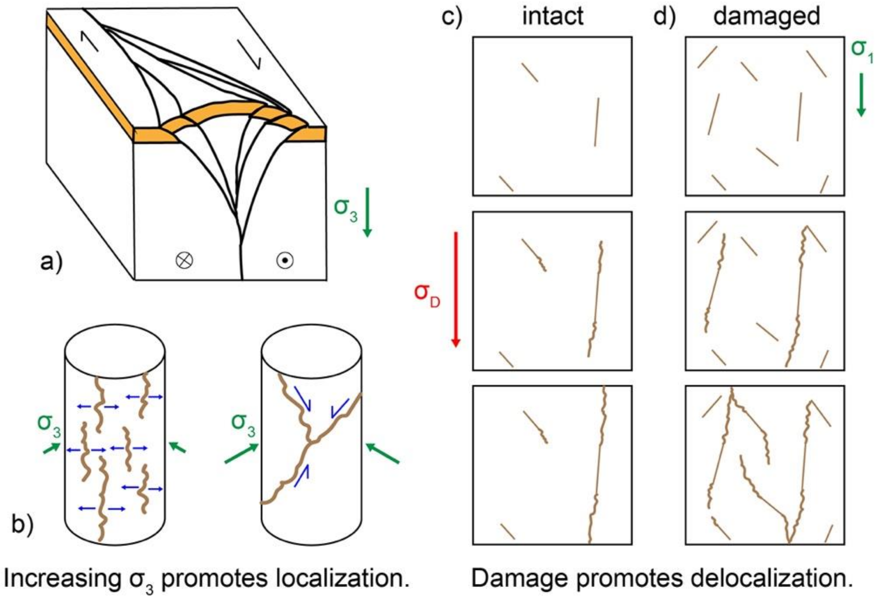

Figure 12. Examples of increasing confining pressure promoting localization (a-b), and preexisting damage promoting delocalization (c-d). a) Positive flower structures that develop along strike-slip fault networks host a diffuse network of fractures at the surface that localize into a narrower zone with depth. b) The tensile-dominated fracture networks that develop under low confining pressure or uniaxial compression tend to be more diffusely spread (left) than the shear-dominated fracture networks that coalesce under higher confining pressure (right). c) With lower amounts of preexisting damage, only a few of the longest and most favorably oriented fractures grow under increasing differential stress. d) With more preexisting damage, several of the smaller fractures may grow, rather than the few longest fractures, thereby producing delocalization.

A network of fractures dominated by shear may be more localized than a network dominated by tension because the stress concentrations that develop at preexisting fractures and heterogeneities may be more important for the coalescence of shear fractures than the propagation of extensile fractures. Because the tensile strength of rocks is lower than the shear strength (Paterson & Wong, 2005 p. 22), extensile fractures may more easily develop throughout the rock core than shear fractures. Shear fractures may thus depend on the stress concentrations that develop near preexisting fractures in order to propagate and coalesce to a greater extent than the extensile fractures. Consequently, the shear fractures may be more likely to develop near preexisting fractures than the extensile fractures, producing more localized fault networks. Consistent with these theoretical arguments, laboratory observations, and crustal observations of fault structures at depth, the present analysis shows that increasing confining pressure promotes greater increases in localization of the high strain events approaching macroscopic failure.

4.3. The influence of preexisting damage on localization approaching macroscopic failure

The present analysis shows that rocks can experience temporary episodes of delocalization, rather than a continuous increase or acceleration of localization toward catastrophic failure (e.g., **Figure 5**). This result is consistent with previous analyses of fracture development (McBeck et al., 2021a) and strain localization (McBeck et al., 2022b) in X-ray tomography triaxial compression experiments. This previous analysis found that the maximum strain localization generally occurs near 90% of the differential stress at macroscopic failure, rather than at macroscopic failure for a range of rock types, including Westerly granite, monzonite, Fontainebleau sandstone, Mount Etna basalt, and Green River shale (McBeck et al., 2022b). In particular, only 46% of the experiments achieve maximum localization at macroscopic failure, or >99% of the failure stress. These results are similar to the damaged rocks in present analysis. For the damaged rocks, the maximum strain localization occurs on average at 94% (contraction), 86% (dilation), and 90% (shear strain) of the differential stress at failure. In contrast, for the intact rocks, the maximum strain localization occurs immediately preceding failure, and on average at 99% (contraction and dilation), and 95% (shear strain) of the differential stress at failure (**Figure 10**).

The results of the previous analysis (McBeck et al., 2022b) may be more consistent with the results of the damaged Westerly granite than the intact Westerly granite because the majority of the experiments used in the previous analysis were performed on rocks with more preexisting pores and fractures than the intact Westerly granite, such as Fontainebleau sandstone and Mt. Etna basalt. The localization behavior of sandstone and basalt is expected to be more similar to damaged Westerly granite than intact Westerly granite because the presence of preexisting damage can influence fracture development (e.g., Helgeson & Aydin, 1991; Tang et al., 2000; d'Alession & Martel, 2004; Gudmundsson et al., 2010; Cartwright-Taylor et al., 2020; Vasseur et al., 2015), and deformation localization (McBeck et al. 2021b). For example, analyses of fracture development in numerical models show that more heterogeneous models produce more precursors than less heterogeneous models (Tang et al., 2000). The precursors in the more heterogeneous models develop in a diffuse distribution early in loading, and then coalesce into a system-spanning fracture that ultimately causes macroscopic failure. In contrast, in less heterogeneous models, only a few precursors develop at random positions throughout the rock, and these positions do not help indicate the final geometry of the system-spanning fracture that causes macroscopic failure. These numerical results are consistent with observations of fracture network development in X-ray tomography triaxial compression experiments on nominally intact and heat-treated (damaged) Ailsa Craig microgranite (Cartwright-Taylor et al., 2020). These experiments show that the heat-treated, and thus more heterogeneous, rock develops more precursory fractures throughout loading toward failure, producing a smooth, continuous evolution, indicative of a second-order transition (Cartwright-Taylor et al., 2020). In contrast, the nominally intact rock hosts few detectable precursors preceding macroscopic failure, producing an abrupt, or first-order, transition. Similarly, numerical models of strike-slip faults embedded in host rock with varying amounts of preexisting weaknesses show that the fracture networks in more homogeneous models continually increase in localization toward macroscopic failure (McBeck et al., 2021b). In contrast, more heterogeneous models experience phases of delocalization superposed on the overall trend of increasing localization. Observations of low-magnitude seismicity preceding several M>7 earthquakes in Southern and Baja California reveal similar phases of delocalization (Ben-Zion & Zaliapin, 2020).

Consistent with the observed influence of heterogeneities on fracture development and localization, the present analysis shows that the damaged Westerly granite experiences maximum localization earlier in loading than the intact Westerly granite (**Figure 10**). Moreover, the proportion of the macroscopic axial strain in which the intact rocks experience localization is larger than the proportion in which the damaged rocks experience localization (**Figure 9**). In addition, the intact rocks tend to experience more cumulative localization throughout loading (**Figure 6**), greater increases in localization immediately preceding failure (**Figure 7**), and smaller v and thus greater absolute localization at failure (**Figure S4**) than the damaged rocks. Thus, more preexisting damage favors delocalization.

The damaged rocks, and more heterogeneous systems in general, may promote episodes of delocalization because the stress concentrations that develop at heterogeneities may allow fracture propagation to require less energy in a network with many smaller fractures than in a more sparsely populated fracture network with several large fractures and only a few smaller fractures (e.g., **Figure 11c**). This effect produces the decreasing strength of rocks at increasing length-scales (e.g., Lockner, 1995; Paterson & Wong, 2005 p. 31). Because larger rock volumes are more likely to contain longer fractures than smaller rock volumes, these longer fractures develop stress concentrations that trigger fracture propagation, and ultimately produce macroscopic failure at a lower level of stress than smaller rock volumes. Consequently, the existence of a diffuse network of heterogeneities enables propagation from many smaller fractures that may delocalize the overall deformation away from the few largest fractures. A diffuse fracture network would also provide a greater opportunity for stress shadows to inhibit growth between fractures (e.g., Nur, 1982) than a more clustered network, and thereby promote delocalization.

5 Conclusions

To assess the influence of confining pressure and preexisting damage on strain localization, we perform a series of X-ray tomography triaxial compression experiments on Westerly granite, and then use digital volume correlation to estimate the local three-dimensional strain tensors throughout loading until macroscopic failure. We examine the evolving volume of the polyhedron that surrounds the highest values of three strain components: the contraction, dilation, and shear strain. We find that experiments with higher confining pressure (>10 MPa) host larger amounts of dilation than experiments with lower confining pressure, consistent with previous laboratory analyses on low porosity crystalline rock (e.g., Brace & Orange, 1968; Crouch, 1970). Higher confining pressure is also associated with larger increases in localization of the high strain events approaching macroscopic failure. This positive correlation between confining pressure and localization is consistent with the localized geometry of the shear-dominated fractures that develop at higher confining pressures compared to the more diffuse arrangement of the extensile-dominated fractures that develop in uniaxial compression (e.g., Paterson, 1958), and with crustal observations of strike-slip fault networks that narrow with depth (e.g., Sylvester, 1988; Rockwell & Ben-Zion, 2007). Tracking the volume of the high strains shows that the strain events do not always systematically increase in localization towards failure, but instead experience phases of delocalization. This result is consistent with previous X-ray tomography triaxial compression experiments (McBeck et al., 2021a; McBeck et al., 2022b), and with observations of low magnitude seismicity in Southern and Baja California (Ben-Zion & Zaliapin, 2020). The amount of preexisting damage controls the extent of the phases of delocalization, and when the rock experiences the greatest localization of the high strain events. The damaged rocks experience longer proportions of the experiment time, in terms of the macroscopic axial strain, in which the strains are delocalizing than the intact rocks. The heat-treated, and thus damaged, Westerly granite experiments host the greatest localization of the high strain events on average near 90% of the differential stress at failure, consistent with strain localization in rocks with some preexisting porosity and heterogeneities, such as Mt. Etna basalt and Fontainebleau sandstone (McBeck et al., 2022b). In contrast, the intact Westerly granite experiments host the greatest localization of the high strain events on average near 99% of the differential stress at failure. In addition, the high strain events localize by larger magnitudes preceding failure in the intact rocks than the damaged rocks. Consequently, more preexisting damage favors delocalization. More preexisting damage may allow more delocalization because the stress concentrations that develop at preexisting heterogeneities periodically enable smaller fractures to propagate, and form stress shadows that inhibit growth. The results show that the dilation hosts more systematic increases in localization towards failure than the shear strain, consistent with a previous digital volume correlation analysis (McBeck et al., 2022b), and that the timing of maximum localization occurs almost exactly at macroscopic failure, consistent with a machine learning analysis that found that the dilative strain helps predict the timing of catastrophic failure better than the shear strain (McBeck et al., 2020a). Consequently, the dilative strain may provide more reliable information about the timing of catastrophic failure than the shear strain.

Acknowledgements

The Research Council of Norway (grant 300435 to JM), U.S. National Science Foundation (grant EAR-2122168 to YBZ) and the European Research Council under the European Union’s Horizon 2020 research and innovation program (grant No. 101019628 BREAK to FR) funded this work. Beamtime was allocated at the European Synchrotron Radiation Facility (Long Term Proposal ES-1190). We thank Clémence Muzelle for technical support on beamline ID19 at ESRF. We thank Editor Yves Bernabé, an Associate Editor, Roberto Emanuele Rizzo, and an anonymous reviewer for suggestions that improved this manuscript.

Open Research

The experimental data (time series of X-ray tomograms) are available on Norstore with DOI 10.11582/2023.00007 (McBeck, 2023).

References

Aben, F. M., Doan, M. L., Mitchell, T. M., Toussaint, R., Reuschlé, T., Fondriest, M., & Renard, F. (2016). Dynamic fracturing by successive coseismic loadings leads to pulverization in active fault zones. Journal of Geophysical Research: Solid Earth, 121(4), 2338-2360.

Akdag, S., Karakus, M., Nguyen, G. D., Taheri, A., & Bruning, T. (2021). Evaluation of the propensity of strain burst in brittle granite based on post-peak energy analysis. Underground Space, 6(1), 1-11.

Basu, A., Mishra, D. A., & Roychowdhury, K. (2013). Rock failure modes under uniaxial compression, Brazilian, and point load tests. Bulletin of Engineering Geology and the Environment, 72, 457-475.

Ben-Zion, Y. and I. Zaliapin, (2019). Spatial variations of rock damage production by earthquakes in southern California, Earth and Planetary Science Letters, 512, 184–193.

Ben-Zion, Y., & Zaliapin, I. (2020). Localization and coalescence of seismicity before large earthquakes. Geophysical Journal International, 223(1), 561-583.

Benson, P. M., Thompson, B. D., Meredith, P. G., Vinciguerra, S., & Young, R. P. (2007). Imaging slow failure in triaxially deformed Etna basalt using 3D acoustic-emission location and X-ray computed tomography. Geophysical Research Letters, 34(3), L03303.

Bieniawski, Z. T. (1967). Mechanism of brittle fracture of rock: Part I. Theory of the fracture process. Part II. Experimental studies; Part III. Fracture in tension and under long-term loading. International Journal of Rock Mechanics and Mining Sciences & Geomechanics Abstracts, 4(4), 395-406.

Brace, W. F. (1978). Volume changes during fracture and frictional sliding: A review. Pure and Applied Geophysics, 116, 603-614.

Brace, W. F., & Orange, A. S. (1968). Electrical resistivity changes in saturated rocks during fracture and frictional sliding. Journal of Geophysical Research, 73(4), 1433-1445.

Brace, W. F., Paulding Jr, B. W., & Scholz, C. H. (1966). Dilatancy in the fracture of crystalline rocks. Journal of Geophysical Research, 71(16), 3939-3953.

Buades, A., Coll, B., & Morel, J. M. (2005). A non-local algorithm for image denoising. In 2005 IEEE Computer Society Conference on Computer Vision and Pattern Recognition (CVPR'05), 2, 60-65.

Cartwright-Taylor, A., Main, I. G., Butler, I. B., Fusseis, F., Flynn, M., & King, A. (2020). Catastrophic failure: how and when? Insights from 4-D in situ x-ray microtomography. Journal of Geophysical Research: Solid Earth, 125(8), e2020JB019642.

Charalampidou, E. M., Hall, S. A., Stanchits, S., Lewis, H., & Viggiani, G. (2011). Characterization of shear and compaction bands in a porous sandstone deformed under triaxial compression. Tectonophysics, 503(1-2), 8-17.

Crouch, S. L. (1970). Experimental determination of volumetric strains in failed rock. In International Journal of Rock Mechanics and Mining Sciences & Geomechanics Abstracts, 7(6), 589-603.

d'Alessio, M. A., & Martel, S. J. (2004). Fault terminations and barriers to fault growth. Journal of Structural Geology, 26(10), 1885-1896.

Feng, X. T., Kong, R., Zhang, X., & Yang, C. (2019). Experimental study of failure differences in hard rock under true triaxial compression. Rock Mechanics and Rock Engineering, 52, 2109-2122.

Fredrich, J. T., & Wong, T. F. (1986). Micromechanics of thermally induced cracking in three crustal rocks. Journal of Geophysical Research: Solid Earth, 91(B12), 12743-12764.

Griffiths, L., Heap, M. J., Baud, P., & Schmittbuhl, J. (2017). Quantification of microcrack characteristics and implications for stiffness and strength of granite. International Journal of Rock Mechanics and Mining Sciences, 100, 138-150.

Gudmundsson, A., Simmenes, T. H., Larsen, B., & Philipp, S. L. (2010). Effects of internal structure and local stresses on fracture propagation, deflection, and arrest in fault zones. Journal of Structural Geology, 32(11), 1643-1655.

Gueydan, F., Précigout, J., & Montesi, L. G. (2014). Strain weakening enables continental plate tectonics. Tectonophysics, 631, 189-196.

Harding, T. P. (1985). Seismic characteristics and identification of negative flower structures, positive flower structures, and positive structural inversion. AAPG bulletin, 69(4), 582-600.

Helgeson, D. E., & Aydin, A. (1991). Characteristics of joint propagation across layer interfaces in sedimentary rocks. Journal of Structural Geology, 13(8), 897-911.

Hu, J., Zeng, P., Yang, D., Wen, G., Xu, X., Ma, S., Zhao, F., & Xiang, R. (2021). Experimental investigation on uniaxial compression mechanical behavior and damage evolution of pre-damaged granite after cyclic loading. Energies, 14(19), 6179.

Jamison, W. R., & Teufel, L. W. (1979). Pore volume changes associated with failure and frictional sliding of a porous sandstone. 20th US Symposium on Rock Mechanics (USRMS). OnePetro.

Le Guerroué, E., & Cobbold, P. R. (2006). Influence of erosion and sedimentation on strike-slip fault systems: insights from analogue models. Journal of Structural Geology, 28(3), 421-430.

Lee, B., & Rathnaweera, T. D. (2016). Stress threshold identification of progressive fracturing in Bukit Timah granite under uniaxial and triaxial stress conditions. Geomechanics and Geophysics for Geo-Energy and Geo-Resources, 2, 301-330.

Lockner, D. A. (1995). Rock failure: Rock Physics and Phase Relations. A Handbook of Physical Constants. Am. Geophys. Union Reference Shelf. Am. Geophys. Union, 127-141.

Lockner, D., Byerlee, J. D., Kuksenko, V., Ponomarev, A., & Sidorin, A. (1991). Quasi-static fault growth and shear fracture energy in granite. Nature, 350(6313), 39-42.

Lyakhovsky, V., Hamiel, Y., & Ben-Zion, Y. (2011). A non-local visco-elastic damage model and dynamic fracturing. Journal of the Mechanics and Physics of Solids, 59(9), 1752-1776.

McBeck, J. (2023). Granite experiments. [Dataset]. Norstore. https://archive.norstore.no/pages/public/datasetDetail.jsf?id=10.11582/2023.00007.

McBeck, J., Aiken, J. M., Ben-Zion, Y., & Renard, F. (2020a). Predicting the proximity to macroscopic failure using local strain populations from dynamic in situ X-ray tomography triaxial compression experiments on rocks. Earth and Planetary Science Letters, 543, 116344.

McBeck, J. A., Aiken, J. M., Mathiesen, J., Ben-Zion, Y., & Renard, F. (2020b). Deformation precursors to catastrophic failure in rocks. Geophysical Research Letters, 47(24), e2020GL090255.

McBeck, J., Ben-Zion, Y., & Renard, F. (2020c). The mixology of precursory strain partitioning approaching brittle failure in rocks. Geophysical Journal International, 221(3), 1856-1872.

McBeck, J., Ben-Zion, Y., & Renard, F. (2021a). Fracture network localization preceding catastrophic failure in triaxial compression experiments on rocks. Frontiers in Earth Science, 9, 778811.

McBeck, J., Ben-Zion, Y., & Renard, F. (2022a). Predicting fault reactivation and macroscopic failure in discrete element method simulations of restraining and releasing step overs. Earth and Planetary Science Letters, 593, 117667.

McBeck, J., Ben-Zion, Y., & Renard, F. (2022b). Volumetric and shear strain localization throughout triaxial compression experiments on rocks. Tectonophysics, 822, 229181.

McBeck, J., Ben-Zion, Y., Zhou, X., & Renard, F. (2021b). The influence of preexisting host rock damage on fault network localization. Journal of Structural Geology, 153, 104471.

McBeck, J. A., Cordonnier, B., Vinciguerra, S., & Renard, F. (2019). Volumetric and shear strain localization in Mt. Etna basalt. Geophysical Research Letters, 46(5), 2425-2433.

McBeck, J., Kobchenko, M., Hall, S. A., Tudisco, E., Cordonnier, B., Meakin, P., & Renard, F. (2018). Investigating the onset of strain localization within anisotropic shale using digital volume correlation of time-resolved X-ray microtomography images. Journal of Geophysical Research: Solid Earth, 123(9), 7509-7528.

Moore, D. E., & Lockner, D. A. (1995). The role of microcracking in shear-fracture propagation in granite. Journal of Structural Geology, 17(1), 95-114.

Mulyukova, E., & Bercovici, D. (2019). The generation of plate tectonics from grains to global scales: A brief review. Tectonics, 38(12), 4058-4076.

Nur, A. (1982). The origin of tensile fracture lineaments. Journal of Structural Geology, 4(1), 31-40.

Paterson, M. S. (1958). Experimental deformation and faulting in Wombeyan marble. Geological Society of America Bulletin, 69(4), 465-476.

Paterson, M. S., & Wong, T. F. (2005). Experimental rock deformation: the brittle field, 348. Berlin: Springer.

Renard, F., Cordonnier, B., Dysthe, D. K., Boller, E., Tafforeau, P., & Rack, A. (2016). A deformation rig for synchrotron microtomography studies of geomaterials under conditions down to 10 km depth in the Earth. Journal of Synchrotron Radiation, 23(4), 1030-1034.

Renard, F., McBeck, J., Kandula, N., Cordonnier, B., Meakin, P., & Ben-Zion, Y. (2019). Volumetric and shear processes in crystalline rock approaching faulting. Proceedings of the National Academy of Sciences, 116(33), 16234-16239.

Rizzo, R. E., Healy, D., Heap, M. J., & Farrell, N. J. (2018). Detecting the Onset of Strain Localization Using Two-Dimensional Wavelet Analysis on Sandstone Deformed at Different Effective Pressures. Journal of Geophysical Research: Solid Earth, 123(12), 10-460.

Rockwell, T. K., & Ben-Zion, Y. (2007). High localization of primary slip zones in large earthquakes from paleoseismic trenches: Observations and implications for earthquake physics. Journal of Geophysical Research: Solid Earth, 112(B10).

Rudnicki, J. W., & Rice, J. R. (1975). Conditions for the localization of deformation in pressure-sensitive dilatant materials. Journal of the Mechanics and Physics of Solids, 23(6), 371-394.

Satoh, T., Shivakumar, K., Nishizawa, O., & Kusunose, K. (1996). Precursory localization and development of microfractures along the ultimate fracture plane in amphibolite under triaxial creep. Geophysical Research Letters, 23(8), 865-868.

Sylvester, A. G. (1988). Strike-slip faults. Geological Society of America Bulletin, 100(11), 1666-1703.

Tang, C. A., Liu, H., Lee, P. K. K., Tsui, Y., & Tham, L. (2000). Numerical studies of the influence of microstructure on rock failure in uniaxial compression—part I: effect of heterogeneity. International Journal of Rock Mechanics and Mining Sciences, 37(4), 555-569.

Tudisco, E., Andò, E., Cailletaud, R., & Hall, S. A. (2017). TomoWarp2: A local digital volume correlation code. SoftwareX, 6, 267-270.

Vasseur, J., Wadsworth, F. B., Lavallée, Y., Bell, A. F., Main, I. G., & Dingwell, D. B. (2015). Heterogeneity: The key to failure forecasting. Scientific Reports, 5(1), 13259.

Wang, Y., Allam, A., & Lin, F. C. (2019). Imaging the fault damage zone of the San Jacinto fault near Anza with ambient noise tomography using a dense nodal array. Geophysical Research Letters, 46(22), 12938-12948.

Wong, T. F., David, C., & Zhu, W. (1997). The transition from brittle faulting to cataclastic flow in porous sandstones: Mechanical deformation. Journal of Geophysical Research: Solid Earth, 102(B2), 3009-3025.

AGU PUBLICATIONS

JGR: Solid Earth

Supporting information for:

The influence of confining pressure and preexisting damage on strain localization in fluid-saturated crystalline rocks at the stress conditions of the upper crust

Jessica McBeck[1], Benoît Cordonnier[2], Yehuda Ben-Zion[3], François Renard[1,4]

[1]Njord Centre, Departments of Physics and Geosciences, University of Oslo, Oslo, Norway.

[2]European Synchrotron Radiation Facility, Grenoble, France

[3]Department of Earth Sciences and Southern California Earthquake Center, University of Southern California, Los Angeles, CA, USA.

[4]Université Grenoble Alpes, Université Savoie Mont Blanc, Université Gustave Eiffel, CNRS, IRD, ISTerre, 38000 Grenoble, France.

Contents of this file

Figures S1 to S5
Table S1

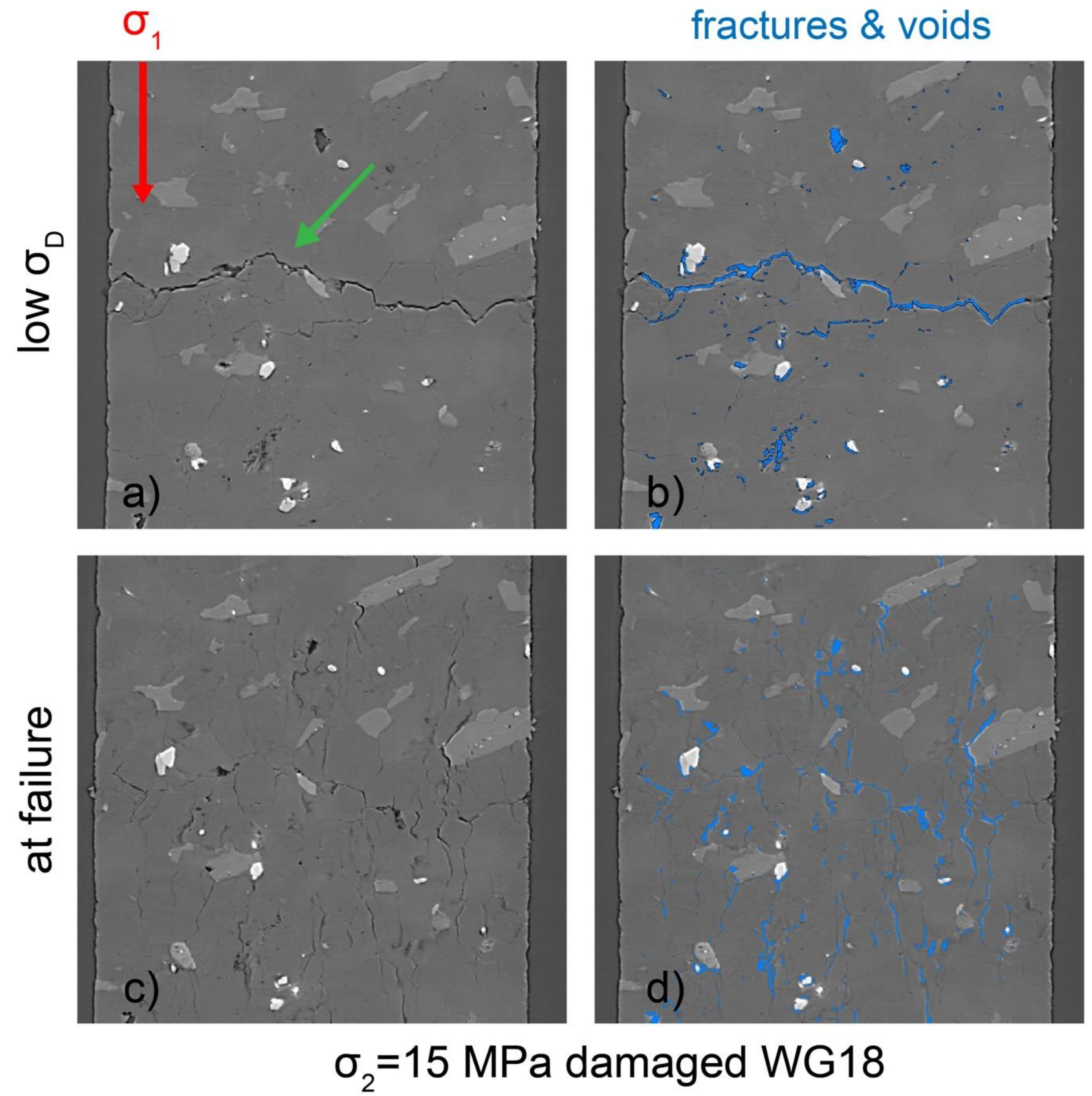

Figure S1. Two-dimensional slices of the tomograms (a, c) and segmented voids and fractures (b, d) in experiment WG18 at lower differential stress, σ_D (a, b), and higher σ_D, immediately preceding macroscopic failure (c, d). This rock core developed a horizontal, core-spanning fracture as it was loaded into the triaxial deformation apparatus, highlighted with a green arrow in (a). With increasing axial and differential stress the fracture closed, producing arrays of mostly vertically-aligned fractures that grew until system-size failure.

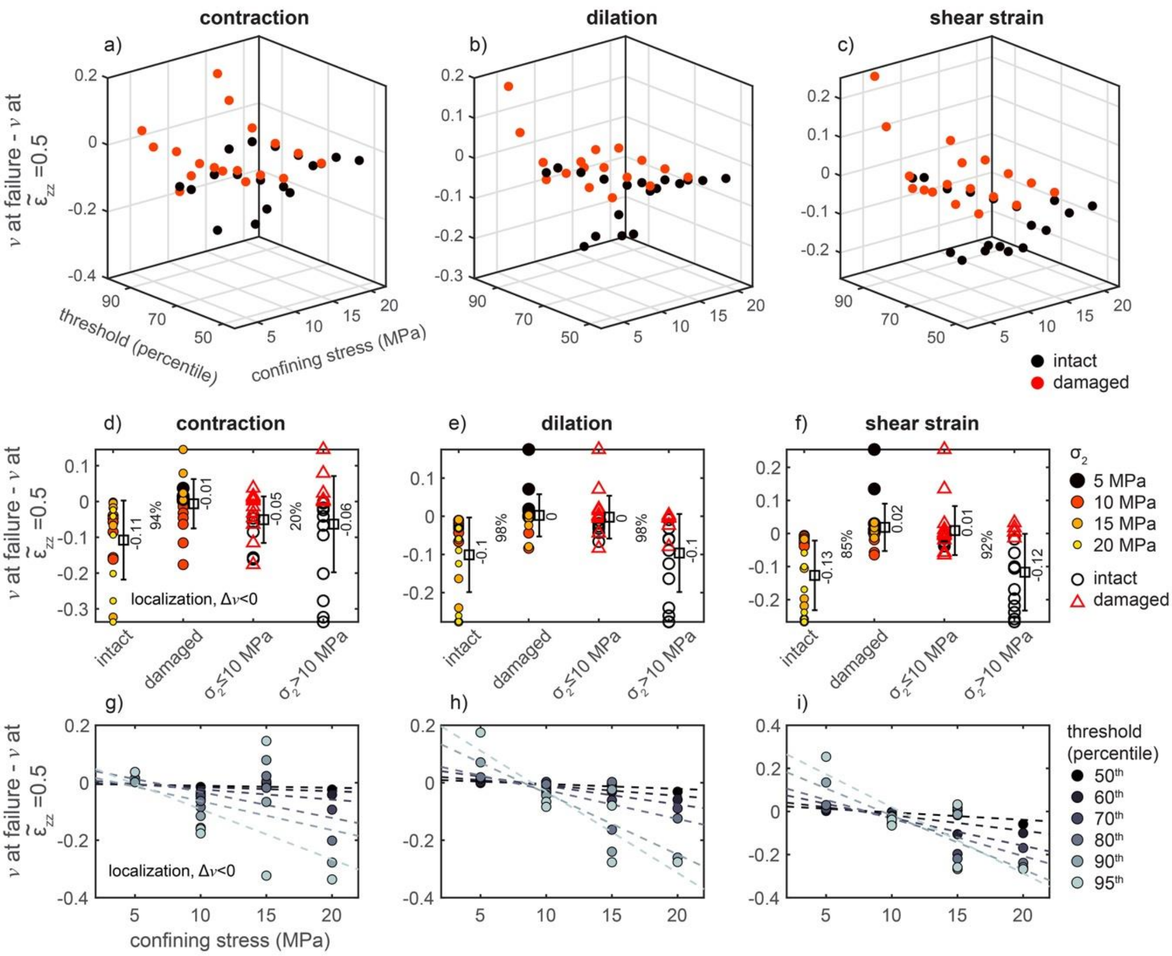

Figure S2. Localization immediately preceding failure measured as the difference in v from the final tomogram acquired immediately preceding failure, when $\widetilde{\varepsilon_{zz}}$ is one, and when $\widetilde{\varepsilon_{zz}}$ is 0.5, Δv. Negative Δv indicates that the high strain events localize towards macroscopic failure. The format of the figure is the same as **Figure 6**.

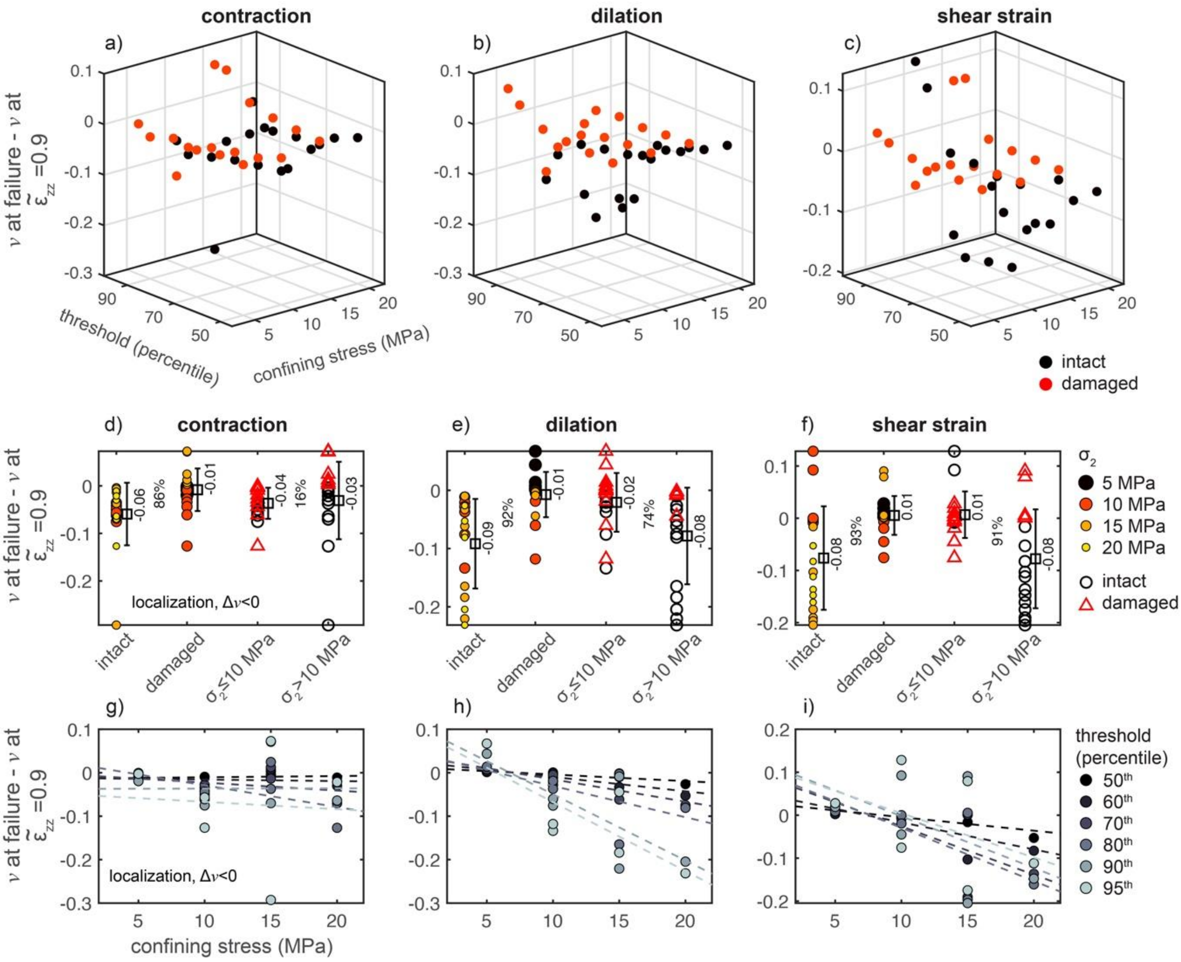

Figure S3. Localization immediately preceding failure measured as the difference in v from the final tomogram acquired immediately preceding failure, when $\widetilde{\varepsilon_{zz}}$ is one, and when $\widetilde{\varepsilon_{zz}}$ is 0.9, Δv. Negative Δv indicates that the high strain events localize towards macroscopic failure. The format of the figure is the same as **Figure 6**.

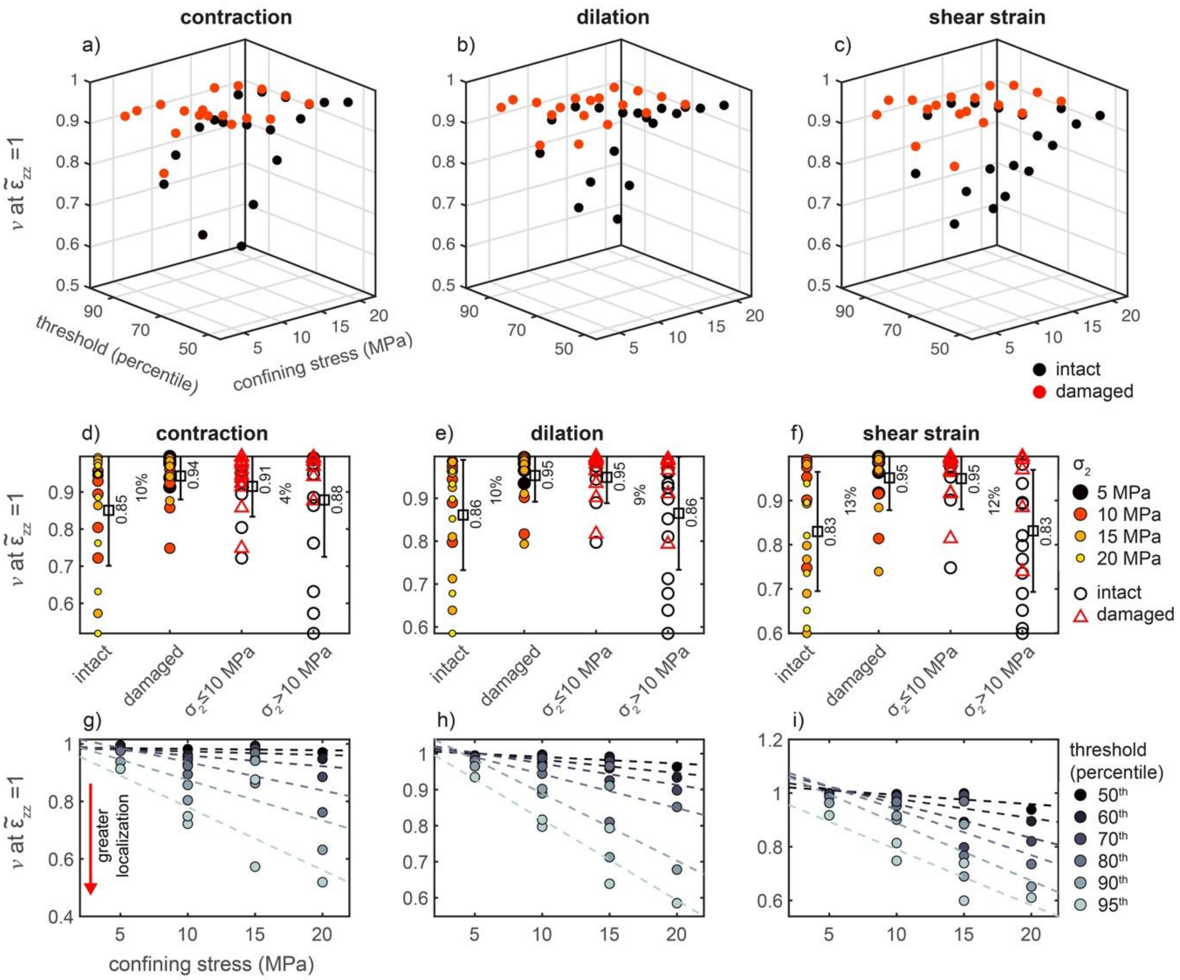

Figure S4. The spatial clustering, ν, of the high strain events immediately preceding failure, when $\widetilde{\varepsilon_{zz}}$ is one. Format is the same as **Figure 6**. The trends shown here are similar to those observed for the cumulative localization (**Figure 6**), and localization from when $\widetilde{\varepsilon_{zz}}$ is 0.5, 0.8 or 0.9, to macroscopic failure (**Figures S2-S3**).

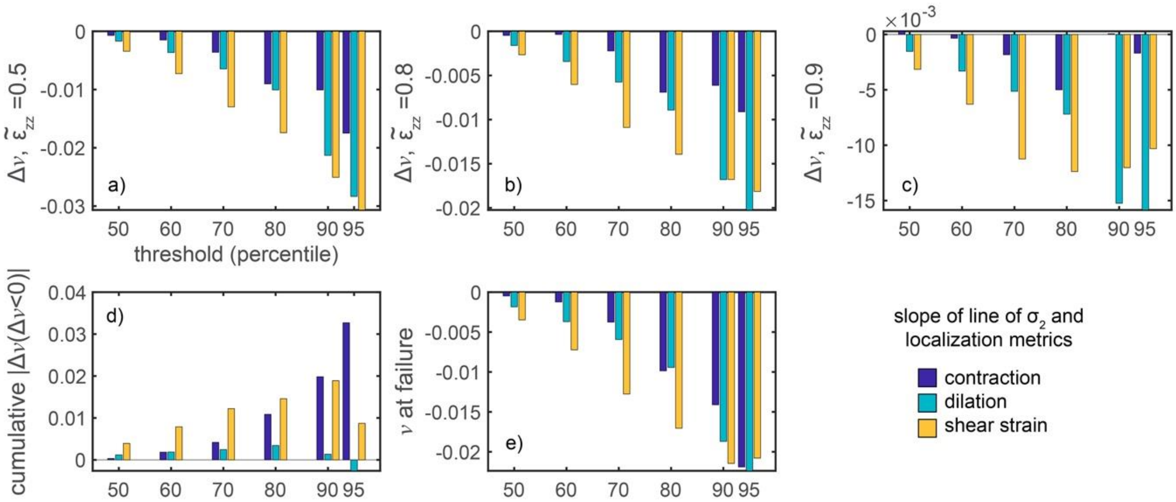

Figure S5. Slopes of the linear fit of different localization metrics for strains >90th percentile and σ_2 of the experiments for each strain component: contraction (dark blue), dilation (light blue), and shear strain (yellow). The horizontal axis indicates strain threshold used to calculate the slope. Each plot shows the slopes for different localization metrics: a-c) $\Delta\nu$ using $\widetilde{\varepsilon_{zz}}$=0.5, $\widetilde{\varepsilon_{zz}}$=0.8, and $\widetilde{\varepsilon_{zz}}$=0.9,

d) the cumulative localization, and e) v at failure. Larger magnitudes indicate a stronger influence of σ_2 on localization. The lines that produce each slope are shown in **Figure** 6, **Figure** 7, **Figure** S2, **Figure** S3, and **Figure** S4.

The confining stress	σ_2
The fluid pressure	P_F
The effective stress, $\sigma_2 - P_f$	P_e
The macroscopic cumulative axial strain measured from the change in height of the rock core observed in the tomograms. We measure the height of the rock core in each tomogram by detecting the interfaces between the top and bottom apparatus pistons and the top and bottom boundaries of the rock core, which are defined by a sharp change in the gray levels of the tomograms, indicative of density.	ε_{zz}
The normalized ε_{zz}. $\widetilde{\varepsilon_{zz}}$ is calculated from the ε_{zz} calculated for the given tomogram, the ε_{zz} of the tomogram acquired immediately preceding macroscopic failure, ε_{zz}^F, and the ε_{zz} of the first tomogram acquired at the onset of the linear phase early in loading, ε_{zz}^0, as $\widetilde{\varepsilon_{zz}} = (\varepsilon_{zz} - \varepsilon_{zz}^0)/(\varepsilon_{zz}^F - \varepsilon_{zz}^0)$	$\widetilde{\varepsilon_{zz}}$
The divergence of the incremental displacement field, the volumetric strain. Negative is contractive and positive is dilative.	$I1$
The second invariant of the deviatoric strain tensor derived from the displacement field, indicative of shear strain.	$J2$
The volume of the polyhedron that surrounds high values of each strain component	v_h
The volume of the polyhedron that surrounds all of the values of the given strain component	v_t
The volume proportion occupied by high strain events, $v = v_h/v_t$	v
The absolute value of the sum of the negative values of the change in v from one digital volume correlation calculation to the next, when $\widetilde{\varepsilon_{zz}}$>0.5, $\sum_{\widetilde{\varepsilon_{zz}}=0.5}^{\widetilde{\varepsilon_{zz}}=1} \lvert\Delta v(\Delta v < 0)\rvert$. Increasing values indicate higher magnitudes of localization.	Cumulative localization
Change in v from DVC calculation *n*+1 to *n*, as $v_{n+1} - v_n$, or change in v from $\widetilde{\varepsilon_{zz}}$=1 to an earlier $\widetilde{\varepsilon_{zz}}$, such as 0.5, 0.8, or 0.9. Negative Δv indicates localization towards macroscopic failure.	Δv

Table S1. Symbols and notation used in the manuscript.